AIMS Mathematics, 11(4): 12233–12286.
DOI: 10.3934/math.2026502
Received: 06 February 2026
Revised: 21 March 2026
Accepted: 13 April 2026
Published: 30 April 2026

http://www.aimspress.com/journal/Math

Research article

Performance enhancement of a 12-pole AMB model via robust control approach

Hany Samih Bauomy*

Department of Mathematics, College of Science and Humanities in Alkharj, Prince Sattam Bin Abdulaziz University, Alkharj 11942, Saudi Arabia

* **Correspondence:** Email: hany_samih@yahoo.com.

Abstract: In this study, I investigated the energetic behavior of a twelve-pole active magnetic bearing (AMB) framework with a nonlinear proportional derivative cubic velocity feedback (NPDCVF) controller in the presence of mixed excitations and primary resonance ($\Omega \cong \omega_1$, $\Omega \cong \omega_2$). The controller combines classic proportional-derivative (PD) control with nonlinear cubic velocity feedback to improve stability, reduce rotor oscillations, and increase robustness. A detailed mathematical framework of the 12-pole AMB system was developed, accounting for magnetic force nonlinearity, dynamic interactions between poles, and the effects of rotor eccentricity. The motion equations (ME) were investigated using the multiple time scales approach (MTSA), and the approximation solutions (AS) were numerically validated with the fourth-order Runge-Kutta (4RK) method. Simulations were performed to compare five controllers: PD, integral resonant controller (IRC), positive position feedback (PPF), nonlinear integral positive position feedback (NIPPF), and the proposed NPDCVF scheme. MATLAB 18.2 numerical simulations (4RK) were employed to analyze time-history responses, the effects of system parameters, and the performance of controllers. The time-domain results showed that the NPDCVF controller delivers the quickest vibration reduction, the least overshoot, and increased robustness to disturbances and parameter changes. Time-domain, frequency-response, and phase-plane analyses confirmed wider stability margins and increased damping effectiveness. Additional nonlinear dynamical assessments, such as bifurcation charts, frequency response curves, and stable and unstable zones, showed that nonlinear oscillations have been successfully reduced and the AMB system has stabilized reliably.

Keywords: vibration suppression; rotor dynamics; AMB; perturbation; stability enhancement

Mathematics Subject Classification: 70K20, 74H45

Abbreviations:

AMB	Active magnetic bearing
NPDCVF	Nonlinear proportional derivative cubic velocity feedback
PD	Proportional-derivative
IRC	Integral resonant controller
PPF	Positive position feedback
NIPPF	Nonlinear integral positive position feedback
MTSA	Multiple time scales approach
4RK	Fourth-order runge-kutta
ME	Motion equations
AS	Approximation solutions
PID	Proportional-integral-derivative
HSFD	Hybrid squeeze film damper
DOF	Degrees of freedom
FRC	Frequency response curves
NCVF	Negative cubic velocity feedback
NPD	Nonlinear proportional-derivative
CVF	Cubic velocity feedback
DSP	Digital signal processor
FPGA	Field programmable gate array
TPPF	Tuned positive position feedback

1. Introduction

By using regulated electromagnetic forces to provide contactless rotor suspension, AMBs have emerged as a crucial part of contemporary high-speed and accurate rotating machinery. AMBs are crucial for turbomachinery, flywheel energy storage systems, vacuum pumps, and aerospace applications because, in contrast to conventional bearings, they provide frictionless functionality, active vibration management, and maintenance-free operation [1–3]. Despite these advantages, AMBs are essentially open-loop unstable and very nonlinear, mostly because of the quadratic relationship between air-gap displacement, coil current, and magnetic force. AMB frameworks are susceptible to external disturbances and changes in structural parameters, particularly when operating in resonant conditions due to the combination of these nonlinearities and the interaction between magnetic poles. Wu et al. [4] showed that a 16-pole leg design and current saturation significantly affect the nonlinear vibrations of the system. Moreover, the AMB framework may experience simultaneous primary and principal parametric resonances when the rotor experiences mixed excitations, such as base motion disruptions and time-varying stiffness impacts from current modulation or field harmonics [5,6]. The dynamic response may rise dramatically in certain circumstances, leading to severe instability, increased oscillations, or the inability to sustain levitation. In nonlinear rotor dynamics, effectively recording and controlling the system response under these combined resonance conditions remains a challenging problem. Studies have shown that subharmonic, super-harmonic, or chaotic oscillations can be caused by small parametric changes or delayed feedback [7,8], underscoring the need for more

complex and adaptive control techniques. Traditional linear controllers like proportional-integral-derivative (PID) and PD are commonly employed for AMB stabilization because of their ease of use and real-time application [9]. However, these controllers are typically built using small-signal linearization assumptions, which results in insufficient robustness and damping under strong nonlinear excitations or resonant conditions. Even though advanced methods like IRC [10], tuned positive position feedback (TPPF) [11], and its nonlinear variations like NIPPF [12] have improved dynamic response and vibration suppression, their performance declines during concurrent resonances when coupling effects and fast changes in system parameters are predominant.

The extensive usage of magnetic bearing systems in engineering has sparked an increased interest in nonlinear control theory. Nonlinear control approaches can enhance dynamic performance and stability by efficiently reducing system vibrations [13,14]. Ji [15] developed a theoretical framework for nonlinear system control by studying the stability and Hopf bifurcation properties of AMB framework with time delay. Using vertical axis PID control, Inoue et al. [16] examined how integral feedback affected the nonlinear vibrations of a stiff rotating shaft and introduced a control method based on nonlinear vibration analysis. A six-degree of freedom (DOF) active magnetic levitation bearing system was controlled by Sung et al. [17] using a powerful fuzzy controller. By examining the control performance, stability requirements, and bifurcation features of a twelve-pole magnetic bearing solution, Zhang et al. [18] created a novel nonlinear time-varying stiffness control method. Wu et al. [19] suggested a global method for bifurcation and chaos control using PD control after studying the dynamic analysis and vibration management of a magnetic bearing system subjected to base motion. A dynamic method and methodology for managing a rotor system with high eccentricity was proposed by Xu et al. [20]. A nonlinear dynamic analysis of a rotor system with a hybrid squeeze film damper (HSFD) experiencing secondary dampening was carried out by Chang et al. [21]. Wang et al. [22] investigated the control of magnetic bearing systems in positive and negative stiffness regimes. Eissa et al. [23] investigated the nonlinear dynamic behaviors of a rotor-AMB system with time-varying stiffness under coupled excitations. Furthermore, when a regularly varying stiffness was present, Amer and Hegazy [24] investigated the nonlinear dynamic behaviors of a rotor-AMB system under simultaneous primary resonance. Kamel and Bauomy [25] investigated the nonlinear vibrations of a rotor-AMB system under parametric excitations using the many scales technique. Zhang et al. [26,27] investigated global bifurcations, chaos, and transient and persistent nonlinear dynamic behaviors in a rotor-active magnetic bearing system with time-varying stiffness. In their analysis of the rotor-AMB system's nonlinear vibrations with eight pole pairs, Yang et al. [28] identified three motion types in two-DOF nonlinear dynamic systems. Much research has been done on the nonlinear dynamics of rotor-AMB systems. The multi-pulse leaping chaotic dynamics of a rotor-AMB system with quadratic and cubic nonlinear components were investigated by Zhang et al. [29]. According to Li et al. [30,31], a rotor-AMB system experiences at least 17, 19, 21, and 22 limit cycles under different regulatory conditions. Awrejcewicz and Dzyubak [32] investigated the chaos and saturation dynamics of vibrations in a rotor supported by magneto hydrodynamic bearings. Saeed et al. [33] developed an analytical approximate solution for a rotor-AMB system that was undergoing primary resonance and 1:1 internal resonance using the method of many scales. Using numerical methods, Inayat-Hussain [34] investigated how geometric coupling affected the bifurcations of a rotor response in AMBs. Saeed and El-Ganaini [35] investigated the use of time-delayed control to lessen the nonlinear vibrations in a Jeffcott rotor system that hangs horizontally. Ghazavi and Sun [36] examined the bifurcation onset delay in magnetic bearing systems using time-dependent stiffness. Ebrahimi et al. [37] investigated the

impact of specific design features on the bifurcation behaviors of a magnetically supported coaxial rotor in the auxiliary bearings.

Researchers have focused on improving the dynamic performance and robustness of rotor AMB systems using various nonlinear and adaptive control strategies. Kandil [38] investigated the nonlinear dynamic behavior, impact suppression, and stability control of rotor AMB systems by comparing fixed and adjustable surplus current strategies. The results demonstrate that adjustable surplus current control significantly enhances stability and suppresses impacts compared to fixed strategies, underlining the effectiveness of adaptive nonlinear control mechanisms. This complements our work, where a novel NPDCVF controller is proposed that not only enlarges stability margins but also suppresses resonance-induced jump phenomena more effectively than conventional linear and nonlinear controllers. Phase-plane analysis can effectively disclose complicated dynamical events under nonlinear control actions, as proved by recent investigations. Moreover, Bauomy et al. [39] demonstrated that adding negative derivative feedback to a two-DOF coupled system dramatically changed the phase-plane topology of the system, resulting in better stability characteristics and bifurcation suppression. Similar to this, phase-plane trajectories were crucial for locating nonlinear resonance, stable attractors, and the transition between periodic and quasi-periodic motions in Abohamer et al.'s [40] investigation of nonlinear oscillations in a lumped mechanical system that included a series spring, piezoelectric device, and feedback controller. These investigations demonstrate that the geometric structure of phase-plane trajectories is where controlled nonlinear interactions are most evident. Furthermore, Amer et al. [41] demonstrated the limitations of solely linear controllers in the presence of severe nonlinearities by offering a thorough examination of nonlinear resonance phenomena and bifurcation characteristics under sophisticated feedback control schemes. Moreover, to reduce large-amplitude oscillations and increase stability margins, this study highlights the importance of adding nonlinear control terms. Last, Ghanem et al. [42] looked at nonlinear control strategies for vibration attenuation in rotating systems and showed that, in comparison to traditional PD-based controllers, hybrid and nonlinear feedback mechanisms can greatly improve resilience and dynamic performance. The findings highlight how velocity-dependent nonlinear factors can effectively reduce sensitivity to parameter fluctuations and mitigate resonance-induced jump occurrences.

Major contributions and novelty of this work

- A new NPDCVF controller is proposed, combining PD control with a cubic velocity feedback term to provide amplitude-dependent damping and improved vibration suppression near resonance under mixed excitations.
- The controller is applied to a fully nonlinear 12-pole AMB model that includes magnetic nonlinearities, inter-pole coupling, and rotor eccentricity features not commonly treated together.
- A nonlinear analytical study using the method of multiple time scales is conducted to reveal the effect of the cubic term on stability and bifurcation behavior.
- Analytical solutions are numerically validated using the 4RK method, confirming the accuracy of the theoretical predictions.
- The controller demonstrates enhanced robustness under mixed excitations, reducing jump phenomena and sensitivity to parameter variations.

- A systematic performance comparison with PD, IRC, PPF, and NIPPF controllers demonstrates the superior vibration suppression and robustness of the proposed NPDCVF scheme.
- A comprehensive nonlinear dynamic model is developed, incorporating magnetic force nonlinearities, inter-pole coupling, and rotor eccentricity effects.
- Advanced nonlinear dynamic analyses, including frequency-response curves, bifurcation diagrams, and stability regions, confirm effective suppression of nonlinear oscillations and enlarged stable operating domains.

By incorporating a nonlinear cubic velocity component for dynamic gain adjustment, the NPDCVF controller, which builds on earlier advancements, enhances the traditional PD architecture. This increases resilience to parameter changes, maximizes transient performance, and enhances vibration damping across a wide frequency range. A comprehensive nonlinear model of a twelve-pole AMB system is developed, accounting for rotor eccentricity, pole interaction, and magnetic force nonlinearity under combined excitations and contemporaneous resonance. NPDCVF significantly reduces overshoot, accelerates vibration fading, and enhances stability margins, according to comparative simulations using PD, IRC, PPF, and NIPPF controllers. In conclusion, the proposed controller provides a very effective and energy-efficient way to keep levitation stable under difficult operating circumstances. The format of the document is as follows: System modeling is covered in Section 2, controller design and stability analysis are explained in Section 3, numerical results are reviewed in Section 4, and the study is concluded in Section 5.

2. Deducing equation of dynamical modeling

In a 12-pole AMB model, two symmetrical drive electromagnets in differential mode generate two opposing magnetic forces. According to the electromagnetic field theory [9], the magnetic force generated between two magnetic poles is

$$F = -\frac{\mu_0 A_0 N^2}{4}\left[\frac{(I_0+I)^2}{(C_0+x)^2} - \frac{(I_0-I)^2}{(C_0-x)^2}\right]. \tag{1}$$

Figure 1 depicts the schematic diagram of a 12-pole AMB framework as it is described in [13]. To accomplish positional control and rotor levitation, the bearing makes use of radial magnetic levitation bearings and electromagnetic coils. While the rotor is aligned, the gap between it and the bearing stays fixed at a particular value. The rotor position is regularly checked by the technology using sensors. To ensure the accuracy and stability of the system, the controller quickly reacts to any deviation by transforming the data into a control signal, which is then amplified to change the rotor's position. A system with twelve magnetic bearings typically has two opposing electromagnetic coils in each pole. Equation (1) can be used to express the electromagnetic force produced by each pair of coils as follows:

$$F_n = -\frac{\mu_0 A_0 N^2}{4}\left[\frac{(I_0+I_n)^2}{(C_0+x_n)^2} - \frac{(I_0-I_n)^2}{(C_0-x_n)^2}\right]\cos\left(\frac{(n-1)\pi}{6}\right), n = 1,2,...,6, \tag{2}$$

where μ_0 signifies the permeability of a vacuum and is used to designate the propagation of magnetic field lines in a vacuum. A_0 symbolizes the cross-sectional area of the electromagnetic core, which

influences the magnetic field strength generated by the electromagnet. N is the number of turns of the electromagnetic coil, which is proportional to the magnetic field strength. x_n is the displacement distance of the bearing rotor during motion, which occurs in a direction. θ is half of the angle between the two opposing magnetic poles. I_0 is the initial bias current applied to the electromagnetic coil, while I_n is the control current applied in the n direction, adjusted according to the feedback from the PD+ (cubic velocity feedback) CVF controllers. Through the reduction or elimination of vibrations brought on by displacement, cubic velocity, and other factors, this feedback and adjustment process guarantees the rotor's stable operation.

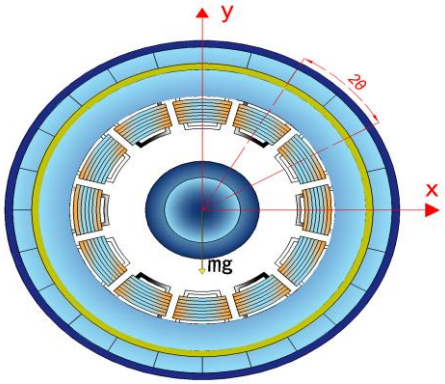

Figure 1. Graph of a 12-pole AMB.

Two opposing electro-magnetic coils are typically found in each pole of a twelve-pole ABM framework. Considering the rotors as rigid bodies, the equations of motion for the rotors can be stated using Newton's theorem as follows, taking into account the rotor's own weight and disregarding fringe flux, eddy current losses, and core material saturation:

$$m\ddot{x} = F_x - c\dot{x} + mr\Omega^2 \cos\Omega t\,, \tag{3}$$

$$m\ddot{y} = F_y - c\dot{y} + mr\Omega^2 \cos\Omega t + mg\,, \tag{4}$$

where x signifies the horizontal displacement of the rotor, F_x symbolizes the electromagnetic force in the horizontal direction, y epitomizes the vertical displacement of the rotor, F_y is the electromagnetic force in the vertical direction, r indicates the eccentricity of the rotor, and Ω signifies the rotor's angular velocity. The control acts on the magnetic bearing are achieved in the prior research using a PD controller. The current is proportionate to the rotor's movement and velocity because the PD controller sets a particular proportional gain k_p and derivative gain k_d. This control technique ensures that the system will respond precisely to the rotor's displacement and velocity [14]. In Figure 1, the weight of the rotor mg acts in the negative vertical direction. This is accounted for in

Eq (4) of motion for the vertical displacement $y(t)$. The term $+mg$ represents the gravitational force acting along the vertical axis, which the electromagnetic force F_y must counteract to maintain stable levitation. Upon analysis of Figure 1, the weight vector mg is depicted as pointing vertically downward. This direction is opposite to the positive direction of the y-axis, which is indicated as pointing vertically upward in the provided coordinate system. Therefore, in terms of vector components, the direction of the weight mg is along the negative y-axis. Specifically, if the positive y-axis is represented by the unit vector j, then the direction of the weight vector can be expressed as -j.

The precise relationship can be articulated.

$$I_n = k_p x_n + k_d \dot{x}_n, n = 1,2,...,6. \tag{5}$$

The PD controller regulates the motion and stability of the magnetic bearing system by acting as a spring with a damping element. The proportional gain coefficient is meant to change frequently throughout time.

$$k_p = k_0 + k_1 \cos(\omega t). \tag{6}$$

We can use coordinate transformation in the 12-pole AMB system to convert the displacement distances x_n in the $6n$ directions into representations in the xy plane coordinate system when thinking of the rotor's displacement as motion in the plane. The rotor's position changes in two-dimensional space are naturally reflected by this method, as demonstrated below:

$$\begin{aligned} &x_1 = x, x_2 = x\cos(30^o) + y\sin(30^o), x_3 = x\cos(60^o) + y\sin(60^o), \\ &x_4 = y, x_5 = x\cos(120^o) + y\sin(120^o), x_6 = x\cos(150^o) + y\sin(150^o). \end{aligned} \tag{7}$$

It is necessary to separate the electromagnetic force F_n produced by each set of electromagnets in the 12-pole AMB framework into two parts: The vertical part F_y and the horizontal part F_x. Using Eq (2), the following equations for F_x and F_y can be produced:

$$F_x = -\frac{\mu_0 A_0 N^2}{4} \sum_{n=1}^{6} \left[\frac{(I_0 + I_n)^2}{(R_0 + x_n)^2} - \frac{(I_0 - I_n)^2}{(R_0 - x_n)^2} \right] \cos\left(\frac{(n-1)\pi}{6} \right), \tag{8}$$

$$F_y = -\frac{\mu_0 A_0 N^2}{4} \sum_{n=1}^{6} \left[\frac{(I_0 + I_n)^2}{(R_0 + x_n)^2} - \frac{(I_0 - I_n)^2}{(R_0 - x_n)^2} \right] \sin\left(\frac{(n-1)\pi}{6} \right). \tag{9}$$

Equation (5) can be combined to yield the formulas that characterize the relationship between F_x and F_y with x and y:

$$F_x = F_1 + F_2\cos(30^0) + F_3\cos(60^0) + F_5\cos(120^0) + F_6\cos(150^0), \tag{10}$$

$$F_y = F_4 + F_2\sin(30^0) + F_3\sin(60^0) + F_5\sin(120^0) + F_6\sin(150^0). \tag{11}$$

Equation (7) can be substituted into Eqs (8) and (9) to yield:

$$\begin{aligned} F_x = {} & 2\sqrt{3}a\left(\frac{(I_0+I_2)^2}{(2R_0+\sqrt{3}x+y)^2} - \frac{(I_0-I_2)^2}{(2R_0-\sqrt{3}x-y)^2} - \frac{(I_0-I_6)^2}{(2R_0-\sqrt{3}x+y)^2} - \frac{(I_0+I_6)^2}{(2R_0+\sqrt{3}x-y)^2}\right) \\ & +2a\left(\frac{(I_0-I_5)^2}{(2R_0+x-\sqrt{3}y)^2} - \frac{(I_0+I_5)^2}{(2R_0-x+\sqrt{3}y)^2} - \frac{(I_0+I_3)^2}{(2R_0+x+\sqrt{3}y)^2} - \frac{(I_0-I_3)^2}{(2R_0-x-\sqrt{3}y)^2}\right) \\ & +a\left(\frac{(I_0+I_1)^2}{(R_0+x)^2} - \frac{(I_0-I_1)^2}{(R_0-x)^2}\right), \end{aligned} \tag{12}$$

$$\begin{aligned} F_y = {} & 2\sqrt{3}a\left(\frac{(I_0+I_2)^2}{(2R_0+\sqrt{3}x+y)^2} - \frac{(I_0-I_2)^2}{(2R_0-\sqrt{3}x-y)^2} - \frac{(I_0-I_6)^2}{(2R_0-\sqrt{3}x+y)^2} - \frac{(I_0+I_6)^2}{(2R_0+\sqrt{3}x-y)^2}\right) \\ & +2a\left(\frac{(I_0-I_5)^2}{(2R_0+x-\sqrt{3}y)^2} - \frac{(I_0+I_5)^2}{(2R_0-x+\sqrt{3}y)^2} - \frac{(I_0+I_3)^2}{(2R_0+x+\sqrt{3}y)^2} - \frac{(I_0-I_3)^2}{(2R_0-x-\sqrt{3}y)^2}\right) \\ & +a\left(\frac{(I_0+I_6)^2}{(R_0+y)^2} - \frac{(I_0-I_6)^2}{(R_0-y)^2}\right), \end{aligned} \tag{13}$$

where $a = \dfrac{\mu_0 A_0 N^2 I_n^2}{4R_0^2}\cos\theta$.

We can complete a Taylor expansion of Eqs (12) and (13) at $x=0$, and $y=0$, respectively, by disregarding the third-order and higher-order terms to obtain the revised electromagnetic force formula. The expression that results is as follows:

$$\begin{aligned} F_x = {} & (\bar{\mu}_1 - 3\bar{\mu}_2 x^2 - 3\bar{\mu}_3 x\dot{x} - \bar{\mu}_2 y^2 - 2\bar{\mu}_3 y\dot{y} + \bar{\mu}_4\dot{y})\dot{x} + (-\bar{\alpha}_1 + \bar{\alpha}_2 x^2 + \bar{\alpha}_3 y^2 + \bar{\alpha}_4 y)x \\ & -(2\bar{\mu}_2 xy + \bar{\mu}_3 x\dot{y} + \bar{\mu}_4 x)\dot{y} - \bar{f}_{11}x\cos\omega t + \bar{f}_{12}xy\cos\omega t, \end{aligned} \tag{14}$$

$$\begin{aligned} F_y = {} & (\bar{\mu}_1 - 3\bar{\mu}_2 y^2 - 3\bar{\mu}_3 y\dot{y} - \bar{\mu}_2 x^2 - 2\bar{\mu}_3 x\dot{x} + \bar{\mu}_4\dot{x})\dot{y} + (-\bar{\beta}_1 + \bar{\beta}_2 y^2 + \bar{\beta}_3 x^2 + \bar{\beta}_4 x)y \\ & -(2\bar{\mu}_2 xy + \bar{\mu}_3 y\dot{x} + \bar{\mu}_4 y)\dot{x} + \bar{f}_{21}y\cos\omega t - \bar{f}_{22}x^2\cos\omega t - \bar{f}_{23}y^2\cos\omega t, \end{aligned} \tag{15}$$

where

$$\begin{aligned} & \bar{\mu}_1 = -\frac{12ak_d}{I_0}, \bar{\mu}_2 = \frac{3ak_d}{R_0^2 I_0^2}(2R_0k_0 - 3I_0), \bar{\mu}_3 = \frac{3ak_d^2}{R_0 I_0^2}, \bar{\mu}_4 = \frac{2a\gamma k_d}{R_0 I_0}(5+3\sqrt{3}), \\ & \bar{\alpha}_1 = \frac{4a}{R_0 I_0}(3R_0k_0 - 3I_0 - 2\gamma^2 I_0), \bar{\alpha}_1 = \frac{3a}{R_0^3 I_0^2}(6I_0^2 - 9R_0 I_0 k_0 + 3R_0^2 k_0^2 + \frac{10}{3}\gamma^2 I_0^2), \end{aligned} \tag{16}$$

$$\bar{\beta}_1=\frac{12a}{R_0I_0}(R_0k_0-(1+\gamma^2)I_0),\bar{\alpha}_3=\bar{\beta}_2=\bar{\beta}_3=\frac{9a}{R_0^3I_0^2}(R_0^2k_0^2-3R_0I_0k_0+2(1+\gamma^2)I_0^2),$$

$$\bar{\alpha}_4=\bar{\beta}_4=\frac{2a\gamma}{R_0^2I_0}((6+2\sqrt{3})R_0k_0-(9+3\sqrt{3})I_0)),\bar{\beta}_5=\frac{a\gamma}{R_0^2I_0}((6\sqrt{3}+10)R_0k_p-(9\sqrt{3}+15)I_0),$$

$$\bar{\beta}_6=4a\gamma(2+\sqrt{3}),\bar{f}_{11}=\frac{12ak_1}{I_0},\bar{f}_{12}=\frac{4a\gamma k_1}{R_0I_0}(3+\sqrt{3}),\bar{f}_{21}=\frac{12ak_1}{I_0},$$

$$\bar{f}_{22}=\frac{a\gamma k_1}{R_0I_0}(2\sqrt{3}+6),\bar{f}_{23}=\frac{a\gamma k_1}{R_0I_0}(6\sqrt{3}+10),$$

where $\gamma=\frac{i_n}{I_0}$.

The motion equation of the 12-pole AMB system can be found by substituting Eq (3) into Eqs (12) and (13):

$$\begin{aligned}m\ddot{x}+(\bar{\mu}_1-c-3\bar{\mu}_2x^2-3\bar{\mu}_3x\dot{x}-\bar{\mu}_2y^2-2\bar{\mu}_3y\dot{y})\dot{x}-(2\bar{\mu}_2xy+\bar{\mu}_3x\dot{y})\dot{y}-\bar{\mu}_4x\dot{y}-\bar{\mu}_4y\dot{x}+\bar{\alpha}_1x\\-\bar{\alpha}_2x^3-\bar{\alpha}_3xy^2-\bar{\alpha}_4yx+\bar{f}_{11}x\cos\omega t-\bar{f}_{12}xy\cos\omega t=mr\Omega^2\cos\Omega t\end{aligned}\tag{17}$$

$$\begin{aligned}m\ddot{y}+(\bar{\mu}_1-c-3\bar{\mu}_2y^2-3\bar{\mu}_3y\dot{y}-\bar{\mu}_2x^2-2\bar{\mu}_3x\dot{x})\dot{y}-(2\bar{\mu}_2xy+\bar{\mu}_3y\dot{x})\dot{x}-\bar{\mu}_4x\dot{x}-\bar{\mu}_4y\dot{y}+\bar{\beta}_1y\\-\bar{\beta}_2y^3-\bar{\beta}_3yx^2-\bar{\beta}_4x^2-\bar{\beta}_5y^2+\bar{f}_{21}y\cos\omega t-(\bar{f}_{22}x^2+\bar{f}_{23}y^2)\cos\omega t=mr\Omega^2\sin\Omega t\end{aligned}\tag{18}$$

Non-dimensionalization makes nonlinear dynamics computations easier. It eases difficult analytical difficulties and makes it easier to compare physical amounts without thinking about units. The following results from adding the dimensionless variables and letting $\bar{\mu}_{10}=\bar{\mu}_1-c$:

$$\begin{aligned}&x^*=\frac{x}{R_0},y^*=\frac{y}{R_0},t^*=t\left(\frac{a}{mR_0}\right)^{\frac{1}{2}},\omega^*=\omega\left(\frac{mR_0}{a}\right)^{\frac{1}{2}},\Omega^*=\Omega\left(\frac{mR_0}{a}\right)^{\frac{1}{2}},\\&\mu_{10}=\bar{\mu}_{10}\left(\frac{R_0}{ma}\right)^{\frac{1}{2}},\mu_2=R_0^2\bar{\mu}_2\left(\frac{R_0}{ma}\right)^{\frac{1}{2}},\mu_3=\bar{\mu}_3\frac{R_0^2}{m},\mu_4=R_0\bar{\mu}_4\left(\frac{R_0}{ma}\right)^{\frac{1}{2}},\\&\mu_5=d_0\bar{\mu}_5\left(\frac{R_0}{ma}\right)^{\frac{1}{2}},\alpha_2=\bar{\alpha}_2\frac{R_0^3}{a},\alpha_3=\bar{\alpha}_3\frac{R_0^3}{a},\alpha_4=\bar{\alpha}_4\frac{R_0^3}{a},F=\frac{mr\Omega^2}{R_0},\\&\omega_1^2=\frac{R_0\bar{\alpha}_1}{a},\omega_1^2=\frac{R_0\bar{\beta}_1}{a},\beta_2=\bar{\beta}_2\frac{R_0^3}{a},\beta_3=\bar{\beta}_3\frac{R_0^3}{a},\beta_4=\bar{\beta}_4\frac{R_0^2}{a},\beta_5=\bar{\beta}_5\frac{R_0^2}{a},\\&f_{12}=\bar{f}_{12}\frac{R_0^2}{a},f_{21}=\bar{f}_{21}\frac{R_0}{2a},f_{11}=\bar{f}_{11}\frac{R_0}{2a},f_{22}=\bar{f}_{22}\frac{R_0^2}{a},f_{23}=\bar{f}_{23}\frac{R_0^2}{a}.\end{aligned}\tag{19}$$

The processed dimensionless motion equations are

$$\ddot{x}+(\bar{\mu}_{10}-3\mu_2x^2-3\mu_3x\dot{x}-\mu_2y^2-2\mu_3y\dot{y}-\mu_4y)\dot{x}-(2\mu_2xy+\mu_3x\dot{y}+\mu_4x)\dot{y}+\omega_1^2x-\alpha_2x^3\tag{20}$$

$$-\alpha_3 xy^2 - \alpha_4 xy + (2f_{11}x - f_{12}xy)\cos\omega t = F\cos\Omega t,$$

$$\begin{aligned}\ddot{y} + (\mu_{10} - 3\mu_2 x^2 - 3\mu_3 x\dot{x} - \mu_2 y^2 - 2\mu_3 x\dot{x} - \mu_5 y)\dot{y} - (2\mu_2 xy + \mu_3 \dot{x}y + \mu_4 x)\dot{x} + \omega_2^2 y - \beta_2 y^3 \\ - \beta_3 x^2 y - \beta_4 x^2 - \beta_5 y^2 + (2f_{21}y - f_{22}x^2 + f_{23}y^2)\cos\omega t = \varepsilon F\sin\Omega t.\end{aligned} \tag{21}$$

3. Equations of the modeling system with perturbation analysis

3.1. Mathematical examination through a perturbation technique

Because of their complex, multi-scale behavior, nonlinear dynamic systems can be difficult to fully understand and describe on a single scale. The dynamic features of these systems can be more thoroughly investigated thanks to the highly effective approximation method known as MTSA. In this work, I apply the resulting scale transformation to proposed Eqs (20) and (21) using the multiple time scale perturbation analysis method [43–46]. A scaling strategy for transformation can be used to investigate the 12-pole AMB system's nonlinear dynamic features in detail. The averaged equations for the system can be obtained by simplifying the analysis process by introducing a small perturbation parameter ε:

$$\begin{aligned}&\mu_{10} \to \varepsilon\mu_{10}, \mu_2 \to \varepsilon\mu_2, \mu_3 \to \varepsilon\mu_3, \mu_4 \to \varepsilon\mu_4, \mu_5 \to \varepsilon\mu_5, \alpha_2 \to \varepsilon\alpha_2, \alpha_3 \to \varepsilon\alpha_3, \alpha_4 \to \varepsilon\alpha_4,\\ &\beta_2 \to \varepsilon\beta_2, \beta_3 \to \varepsilon\beta_3, \beta_4 \to \varepsilon\beta_4, \beta_5 \to \varepsilon\beta_5, f_{11} \to \varepsilon f_{11}, f_{12} \to \varepsilon f_{12}, f_{21} \to \varepsilon f_{21},\\ &f_{22} \to \varepsilon f_{22}, f_{23} \to \varepsilon f_{23}, F \to \varepsilon F.\end{aligned} \tag{22}$$

The small perturbation parameter is introduced to represent the weakly nonlinear nature of the system, reflecting realistic operating conditions of active magnetic bearings where rotor displacements, control forces, and nonlinear magnetic effects remain small relative to their nominal values. This assumption enables the application of the method of multiple scales while preserving the dominant nonlinear interactions relevant to resonance phenomena.

Equation (22) is substituted into Eqs (20) and (21) to get the scaled dynamic control equations for the 12-pole AMB framework after I change these equations by adding a parametric excitation force:

$$\begin{aligned}&\ddot{x} + \varepsilon(\mu_{10} - 3\mu_2 x^2 - 3\mu_3 x\dot{x} - \mu_2 y^2 - 2\mu_3 y\dot{y})\dot{x} - \varepsilon(2\mu_2 xy + \mu_3 x\dot{y})\dot{y} - \varepsilon\mu_4(x\dot{y} - \dot{x}y) + \omega_1^2 x\\ &-\varepsilon\alpha_2 x^3 - \varepsilon\alpha_3 xy^2 - \varepsilon\alpha_4 xy + 2\varepsilon f_{11}x\cos\omega t - \varepsilon f_{12}xy\cos\omega t = \varepsilon F\cos\Omega t + \varepsilon F x\cos\Omega t,\end{aligned} \tag{23}$$

$$\begin{aligned}&\ddot{y} + \varepsilon(\mu_{10} - 3\mu_2 x^2 - 3\mu_3 x\dot{x} - \mu_2 y^2 - 2\mu_3 x\dot{x})\dot{y} - \varepsilon(2\mu_2 xy + \mu_3 \dot{x}y)\dot{x} - \varepsilon\mu_4 x\dot{x} - \varepsilon\mu_5 y\dot{y} + \omega_2^2 y\\ &-\varepsilon\beta_2 y^3 - \varepsilon\beta_3 x^2 y - \varepsilon\beta_4 x^2 - \varepsilon\beta_5 y^2 - \varepsilon(-2f_{21}y + f_{22}x^2 + f_{23}y^2)\cos\omega t = \varepsilon F\sin\Omega t + \varepsilon F y\sin\Omega t.\end{aligned} \tag{24}$$

Negative cubic velocity feedback (NCVF) with nonlinear proportional-derivative (NPD), added as a novel controller NPDCVF in the simultaneous resonance scenario postulated by ($\Omega \cong \omega_1$, $\Omega \cong \omega_2$), is provided by

$$\begin{aligned}&\ddot{x} + \varepsilon(\mu_{10} - 3\mu_2 x^2 - 3\mu_3 x\dot{x} - \mu_2 y^2 - 2\mu_3 y\dot{y})\dot{x} - \varepsilon(2\mu_2 xy + \mu_3 x\dot{y})\dot{y} - \varepsilon\mu_4(x\dot{y} - \dot{x}y) + \omega_1^2 x\\ &-\varepsilon\alpha_2 x^3 - \varepsilon\alpha_3 xy^2 - \varepsilon\alpha_4 xy + 2\varepsilon f_{11}x\cos\omega t - \varepsilon f_{12}xy\cos\omega t = \varepsilon F\cos\Omega t\end{aligned} \tag{25}$$

$$+\varepsilon F x\cos\Omega t+F_{1c}(t),$$

$$\begin{aligned}&\ddot{y}+\varepsilon(\mu_{10}-3\mu_2x^2-3\mu_3x\dot{x}-\mu_2y^2-2\mu_3x\dot{x})\dot{y}-\varepsilon(2\mu_2xy+\mu_3\dot{x}y)\dot{x}-\varepsilon\mu_4x\dot{x}-\varepsilon\mu_5y\dot{y}+\omega_2^2y\\&-\varepsilon\beta_2y^3-\varepsilon\beta_3x^2y-\varepsilon\beta_4x^2-\varepsilon\beta_5y^2+\varepsilon(2f_{21}y-f_{22}x^2-f_{23}y^2)\cos\omega t=\varepsilon F\sin\Omega t\\&+\varepsilon F y\sin\Omega t+F_{2c}(t),\end{aligned}\tag{26}$$

where $F_{1c}(t)$ and $F_{2c}(t)$ are the control inputs, assumed by:

$$F_{1c}(t)=-\varepsilon(p_1x+\mathrm{d}_1\dot{x}+\alpha_5x^3+\alpha_6x^2\dot{x}+\alpha_7x\dot{x}^2+\mathrm{G}_1\dot{x}^3),\tag{27}$$

$$F_{2c}(t)=-\varepsilon(p_2y+\mathrm{d}_2\dot{y}+\beta_6y^3+\beta_7y^2\dot{y}+\beta_8y\dot{y}^2+\mathrm{G}_2\dot{y}^3),\tag{28}$$

where $-(p_1x+\mathrm{d}_1\dot{x}),-(p_2y+\mathrm{d}_2\dot{y})$ remain the linear control forces, $-(\alpha_5x^3+\alpha_6x^2\dot{x}+\alpha_7x\dot{x}^2),-(\beta_6y^3+\beta_7y^2\dot{y}+\beta_8y\dot{y}^2)$ are the non-linear control forces, and G_1,G_2 are the gains.

We can look for a first-order approximate solution for Eqs (25) and (26) using Eqs (27) and (28) via the MTSA [43-46] in the manner described below:

$$x(t;\varepsilon)=x_0(T_0,T_1)+\varepsilon x_1(T_0,T_1)+O(\varepsilon^2),\tag{29a}$$

$$y(t;\varepsilon)=y_0(T_0,T_1)+\varepsilon y_1(T_0,T_1)+O(\varepsilon^2).\tag{29b}$$

The following provides the time-related derivatives:

$$\frac{d}{dt}=D_0+\varepsilon D_1,\ \frac{d^2}{dt^2}=D_0^2+2\varepsilon D_0D_1,\tag{30}$$

where $T_n=\varepsilon^nt(n=0,1)$, and T_0 and T_1 are the fast and slow time scales, respectively. Replacing Eq (29) into Eqs (25) and (26) using Eq (30), I can compare the coefficients of comparable power of ε on both sides to obtain:

$$O(\varepsilon):(D_0^2+\omega_1^2)x_0=0,\tag{31a}$$

$$(D_0^2+\omega_2^2)y_0=0,\tag{31b}$$

$$\begin{aligned}O(\varepsilon^1):(D_0^2+\omega_1^2)x_1=&-2D_0D_1x_0-(\mu_{10}-3\mu_2x_0^2-3\mu_3x_0D_0x_0-\mu_2y_0^2-2\mu_3y_0D_0y_0)D_0x_0+\alpha_2x_0^3\\&+(2\mu_2x_0y_0+\mu_3x_0D_0y_0)D_0y_0+\mu_4x_0D_0y_0+\mu_4y_0D_0x_0+2f_{11}x_0\cos\omega t\\&+\alpha_3x_0y_0^2+\alpha_4x_0y_0+f_{12}x_0y_0\cos\omega t+F\cos\Omega t+Fx_0\cos\Omega t\\&-p_1x_0-d_1D_0x_0-\alpha_5x_0^3-\alpha_6x_0^2D_0x_0-\alpha_7x_0\left(D_0x_0\right)^2-G_1(D_0x_0)^3,\end{aligned}\tag{32a}$$

$$
\begin{aligned}
(D_0^2+\omega_2^2)y_1 = &-2D_0D_1y_0-(\mu_{10}-3\mu_2y_0^2-3\mu_3y_0D_0y_0-\mu_2x_0^2-2\mu_3x_0D_0x_0)D_0y_0+\beta_2y_0^3\\
&+(2\mu_2x_0y_0+\mu_3y_0D_0x_0)D_0x_0+\mu_4y_0D_0x_0+\mu_4x_0D_0y_0+2f_{21}y_0\cos\omega t\\
&+\beta_3y_0x_0^2+\beta_4x_0^2+\beta_5y_0^2+(f_{22}x_0^2+f_{23}y_0^2)\cos\omega t+F\sin\Omega t+Fy_0\sin\Omega t\\
&-p_2y_0-d_2D_0y_0-\beta_6y_0^3-\beta_7y_0^2D_0y_0-\beta_8y_0\left(D_0y_0\right)^2-G_2(D_0y_0)^3 \ .
\end{aligned}
\tag{32b}
$$

The following formula provides the solution to Eq (31):

$$x_0 = A_1e^{i\omega_1T_0}+cc\ , \tag{33a}$$

$$y_0 = A_2e^{i\omega_2T_0}+cc\ , \tag{33b}$$

where A_1 and A_2 denote a complex function that has been validated by eliminating secular and small-divisor terms from the initial estimates. Additionally, this displays the intricate conjugates of the preceding phrases. The specific solutions of Eq (32), after removing Eqs (33), (32), and the secular factors, are as follows:

$$
\begin{aligned}
x_1 = &E_1e^{3i\omega_1T_0}+E_2e^{i(\omega_1+\omega_2)T_0}+E_3e^{i(\omega_1+2\omega_2)T_0}+E_4e^{i(\omega_1+\omega)T_0}+E_5e^{i(\omega_1-\omega)T_0}+E_6e^{i(\omega_1+\omega_2+\omega)T_0}\\
&+E_7e^{i(\omega_1+\omega_2-\omega)T_0}+E_8e^{i\Omega T_0}+E_9e^{i(\Omega+\omega_1)T_0}+E_{10}e^{i(\Omega-\omega_1)T_0}+cc\ ,
\end{aligned}
\tag{34a}
$$

$$
\begin{aligned}
y_1 = &H_1e^{2i\omega_2T_0}+H_2e^{3i\omega_2T_0}+H_3e^{i(\omega_1+\omega_2)T_0}+H_4e^{i(\omega_2+2\omega_1)T_0}+H_5e^{i(\omega_2+\omega)T_0}+H_6e^{i(\omega_2-\omega)T_0}\\
&+H_7e^{i2\omega_1T_0}+H_8e^{i\Omega T_0}+H_9e^{i(\Omega+\omega_2)T_0}+H_{10}e^{i(\Omega-\omega_2)T_0}+H_{11}e^{i(2\omega_1+\omega)T_0}\\
&+H_{12}e^{i(2\omega_1-\omega)T_0}++H_{13}e^{i(2\omega_2+\omega)T_0}+H_{14}e^{i(2\omega_2-\omega)T_0}+cc\ .
\end{aligned}
\tag{34b}
$$

For the purpose of conciseness, the difficult functions where $E_i(i=1,2,...,10)$ and $H_i(i=1,2,...,14)$ are complex functions in T_1, and are not written here. I separate and arrange each resonance scenario from the previously given solutions as follows:

• Primary resonance: $\Omega\cong\omega_n,\ \omega\cong\omega_n,\ n=1,2$,

• Sub-harmonic resonance: $\omega\cong2\omega_n,\ n=1,2$,

• Internal resonance: $\omega_1\cong\omega_2,\omega_1\cong2\omega_2,\omega_2\cong2\omega_1$,

• Combined resonance: $\omega\cong\pm\omega_2\pm\omega_1$.

3.2. Stability examination

We statistically examine every resonance scenario and demonstrate that the simultaneous primary and principle parametric in the presence of primary resonance case, which is provided via $\Omega\cong\omega_1$, $\Omega\cong\omega_2$, is the worst situation. The small-divisor terms are converted hooked on secular terms

by inserting the detuning parameters, σ_1 and σ_2 in accordance with:

$$\Omega \cong \omega_1 + \varepsilon\sigma_1, \Omega \cong \omega_2 + \varepsilon\sigma_2 . \tag{35}$$

The detuning parameters are defined to quantify small deviations of the excitation frequency from the natural frequency of the rotor–bearing system. Their scaling with the perturbation parameter ensures that primary resonance and internal resonance conditions are captured accurately without violating the asymptotic ordering of the perturbation analysis. This choice is standard in nonlinear vibration analysis and enables consistent derivation of modulation equations governing amplitude and phase evolution.

The solvability conditions for the first order approximations are obtained by substituting Eq (35) into Eq (32), and removing the secular terms. I observe that A_1 and A_2 are functions in T_1 , so I acquire:

$$\begin{aligned} 2i\omega_1 D_1 A_1 = &-i\omega_1\mu_{10}A_1 - 3i\omega_1\mu_2 A_1^2\bar{A}_1 - 3\omega_1^2\mu_3 A_1^2\bar{A}_1 + 3\alpha_2 A_1^2\bar{A}_1 + \frac{F}{2}e^{i\sigma_1 T_1} \\ &- p_1 A_1 - i\omega_1 d_1 A_1 - 3\alpha_5 A_1^2\bar{A}_1 - i\omega_1\alpha_6 A_1^2\bar{A}_1 - \alpha_7\omega_1^2 A_1^2\bar{A}_1 - 3iG_1\omega_1^3 A_1^2\bar{A}_1, \end{aligned} \tag{36a}$$

$$\begin{aligned} 2i\omega_2 D_1 B_1 = &-i\omega_2\mu_{10}A_2 - 3i\omega_2\mu_2 A_2^2\bar{A}_2 - 3\omega_2^2\mu_3 A_2^2\bar{A}_2 + 3\beta_2 A_2^2\bar{A}_2 + \frac{F}{2}e^{i\sigma_2 T_1} \\ &- p_2 A_2 - i\omega_2 d_2 A_2 - 3\beta_6 A_2^2\bar{A}_2 - i\omega_2\beta_7 A_2^2\bar{A}_2 - \beta_8\omega_2^2 A_2^2\bar{A}_2 - 3iG_2\omega_2^3 A_2^2\bar{A}_2 . \end{aligned} \tag{36b}$$

Let definite A_1, A_2 and $\bar{A}_1, \bar{A}_2$ be expressed in the resulting polar expressions to distinguish the averaging conditions that provide the components of Eq (36).

$$A_1 = \frac{1}{2}a_1(T_1)e^{i\gamma_1(T_1)} \quad , \qquad \bar{A}_1 = \frac{1}{2}a_1(T_1)e^{-i\gamma_1(T_1)}, \tag{37a}$$

$$A_2 = \frac{1}{2}a_2(T_1)e^{i\gamma_2(T_1)} \quad , \qquad \bar{A}_2 = \frac{1}{2}a_2(T_1)e^{-i\gamma_2(T_1)}, \tag{37b}$$

where the steady-state amplitudes and phases are represented by a_1, a_2, and γ_1, γ_2, respectively. After replacing Eq (37) in Eq (36), separate the imaginary and real components are as follows:

$$a_1' = -\frac{1}{8}\left[\alpha_6 - 3\mu_2 + 3G_1\omega_1^2\right]a_1^3 - \frac{1}{2}\left[\mu_{10} + d_1\right]a_1 + \frac{F}{2\omega_1}\sin\theta_1, \tag{38a}$$

$$a_1\gamma_1' = -\left[\frac{3\omega_1}{8}\mu_3 + \frac{3}{8\omega_1}\alpha_2 + \frac{3}{8\omega_1}\alpha_5 + \frac{\omega_1}{8}\alpha_7\right]a_1^3 - \frac{p_1}{2\omega_1}a_1 - \frac{F}{2\omega_1}\cos\theta_1, \tag{38b}$$

$$a_2' = -\frac{1}{8}\left[\beta_7 - 3\mu_2 + 3G_2\omega_2^2\right]a_2^3 - \frac{1}{2}\left[\mu_{10} + d_2\right]a_2 + \frac{F}{2\omega_2}\sin\theta_2, \tag{39a}$$

$$a_2\gamma_2' = -\left[\frac{3\omega_2}{8}\mu_3 + \frac{3}{8\omega_2}\beta_2 + \frac{3}{8\omega_2}\beta_6 + \frac{\omega_2}{8}\beta_8\right]a_2^3 - \frac{p_2}{2\omega_2}a_2 + \frac{F}{2\omega_2}\cos\theta_2\ , \tag{39b}$$

where

$$\theta_1 = \sigma_1 T_1 - \gamma_1\,,\ \theta_2 = \sigma_2 T_1 - \gamma_2\ . \tag{40}$$

For steady-state responses ($a_1' = a_2' = \theta_1' = \theta_2' = 0$). Then from Eq (30), I acquire:

$$\gamma_1' = \sigma_1\,,\ \gamma_2' = \sigma_2\,. \tag{41}$$

Equations (38) and (39) yield the steady state solutions, which are as follows:

$$-\frac{1}{8}\left[\alpha_6 - 3\mu_2 + 3G_1\omega_1^2\right]a_1^3 - \frac{1}{2}\left[\mu_{10} + d_1\right]a_1 + \frac{F}{2\omega_1}\sin\theta_1 = 0\,, \tag{42a}$$

$$a_1\sigma_1 + \left[\frac{3\omega_1}{8}\mu_3 + \frac{3}{8\omega_1}\alpha_2 + \frac{3}{8\omega_1}\alpha_5 + \frac{\omega_1}{8}\alpha_7\right]a_1^3 + \frac{p_1}{2\omega_1}a_1 + \frac{F}{2\omega_1}\cos\theta_1\,, \tag{42b}$$

$$-\frac{1}{8}\left[\beta_7 - 3\mu_2 + 3G_2\omega_2^2\right]a_2^3 - \frac{1}{2}\left[\mu_{10} + d_2\right]a_2 + \frac{F}{2\omega_2}\sin\theta_2 = 0\,, \tag{43a}$$

$$a_2\sigma_2 + \left[\frac{3\omega_2}{8}\mu_3 + \frac{3}{8\omega_2}\beta_2 + \frac{3}{8\omega_2}\beta_6 + \frac{\omega_2}{8}\beta_8\right]a_2^3 + \frac{p_2}{2\omega_2}a_2 - \frac{F}{2\omega_2}\cos\theta_2 \ne\ . \tag{43b}$$

The first Lyapunov technique is used to determine the eigenvalues of the right-hand side of the Jacobian matrix associated with Eqs (38) and (39) to evaluate the stability of the steady-state structure:

$$\begin{bmatrix} a_1' \\ \gamma_1' \\ a_2' \\ \gamma_2' \end{bmatrix} = \begin{bmatrix} R_{11} & R_{12} & R_{13} & R_{14} \\ R_{21} & R_{22} & R_{23} & R_{24} \\ R_{31} & R_{32} & R_{33} & R_{34} \\ R_{41} & R_{42} & R_{43} & R_{44} \end{bmatrix} \begin{bmatrix} a_1 \\ \gamma_1 \\ a_2 \\ \gamma_2 \end{bmatrix}. \tag{44}$$

Appendix A contains the definitions of the factors $R_{jk} : j = 1,2,3,4, k = 1,2,3,4$. The previous matrix solves the following determinant to obtain the stable areas of the controlled model:

$$\begin{vmatrix} R_{11} - \lambda & R_{12} & R_{13} & R_{14} \\ R_{21} & R_{22} - \lambda & R_{23} & R_{24} \\ R_{31} & R_{32} & R_{33} - \lambda & R_{34} \\ R_{41} & R_{42} & R_{43} & R_{44} - \lambda \end{vmatrix} = 0\,. \tag{45}$$

Then,

$$\lambda^4 + \rho_1\lambda^3 + \rho_2\lambda^2 + \rho_3\lambda + \rho_4 = 0\,, \tag{46}$$

where λ denotes the eigenvalue of the Jacobian matrix, and ρ_1, ρ_2, ρ_3, and ρ_4 denote the coefficients of Eq (46), which are presented in Appendix . According to the Routh-Hurwitz criterion, the structure must meet the following necessary and sufficient characteristics in order to be stable:

$$\rho_1 > 0,\ \rho_1\rho_2 - \rho_3 > 0,\ \rho_3(\rho_1\rho_2 - \rho_3) - \rho_1^2\rho_4 > 0,\quad \rho_4 > 0. \tag{47}$$

3.3. Time-domain displacement response

To evaluate the effectiveness of the proposed NPDCVF scheme, the time-domain displacement responses in $x(t)$ and $y(t)$ directions are examined under identical excitation and operating conditions. Figure 2 illustrates the time-domain displacement responses of the twelve-pole AMB framework before and after applying the NPDCVF controller within primary case $\Omega \cong \omega_1, \Omega \cong \omega_2$. In the uncontrolled case, the rotor exhibits large-amplitude oscillations due to resonance, indicating poor damping and unstable vibration behavior. After activating the NPDCVF controller, the displacement responses in both directions are significantly attenuated and confined near the equilibrium position. The controlled responses demonstrate rapid vibration suppression, reduced oscillation amplitudes, and improved stability over the entire simulation time. These results confirm the strong damping capability and robustness of the NPDCVF controller in mitigating resonance-induced vibrations. Moreover, the controlled signals remain consistently bounded over the 500-second interval, with no signs of drift or amplitude growth. This behavior reflects the robustness and stability of the NPDCVF strategy under long-duration operation and nonlinear excitation. These findings further validate the suitability of the NPDCVF scheme for high-precision rotor stabilization in nonlinear magnetic bearing systems.

Figure 3 provides a deeper understanding of the system's dynamics by showing the relationship between displacement and its corresponding velocity for x and y components. This is crucial for assessing the energy dissipation and stability of the system.

Uncontrolled case (Red):

The trajectories spiral outward from the origin, representing the transient growth of the oscillations. They converge to a limit cycle, appearing as a stable closed loop in the displacement-velocity plane. This indicates sustained oscillations with constant amplitude and frequency. The maximum velocity for the x component is approximately 3.5 units, while for the y component, it reaches about 5.0 units, corresponding to the maximum rates of change in displacement.

NPDCVF controlled case (Blue):

The control system effectively "shrinks" the phase plane trajectory toward the origin. Displacement and velocity are maintained at very low levels, demonstrating the efficiency of the velocity feedback control in damping the system's energy and bringing it to a near-equilibrium state. Finally, the phase plane analysis demonstrates the significant impact of the NPDCVF control strategy. In the uncontrolled scenario, the system exhibits large-amplitude limit cycle oscillations, indicating an

unstable or marginally stable behavior. Conversely, with the NPDCVF control engaged, the system's trajectories are effectively driven toward the origin in displacement-displacement and displacement-velocity phase planes, signifying a highly stable and well-damped response. This highlights the robustness and effectiveness of the NPDCVF controller in mitigating unwanted oscillations and stabilizing the system. The NPDCVF controller gains in this study are chosen based on stability criteria and the literature and then fine-tuned numerically to achieve optimal vibration suppression under the simulated conditions. The time-domain displacement curves have been re-plotted for the requested domain of 0 to 30 seconds. This shorter interval highlights the rapid transient response and damping effectiveness of the NPDCVF controller compared to the uncontrolled growth of oscillations, as plotted in Figure 4. Figures 2–4 are prepared at the selected values:

$$\mu_{10}=0.4,\mu_2=0.25,\mu_3=0.05,\mu_4=0.1,\omega_1=2.0,\alpha_2=0.24,\alpha_3=0.02,\alpha_4=0.04,f_{11}=1.5,\omega=0.6,f_{12}=2.3,$$

$$F=0.5,\Omega=\omega_1,p_1=0.2,d_1=0.12,\alpha_5=0.45,\alpha_6=0.8,\alpha_7=0.6,G_1=0.35,\mu_5=0.15,\omega_2=2.0,\beta_2=0.23,$$

$$\beta_3=0.05,\beta_4=0.08,\beta_5=0.15,f_{21}=0.6,f_{22}=1.1,f_{23}=2.3,\Omega=\omega_2,p_2=0.025,d_2=0.36,\beta_6=0.03,\beta_7=0.33,$$

$$\beta_8=0.45,G_2=1.0,\varepsilon=0.05,x(0)=0,\dot{x}(0)=0.5,y(0)=0,\dot{y}(0)=0.5\,.$$

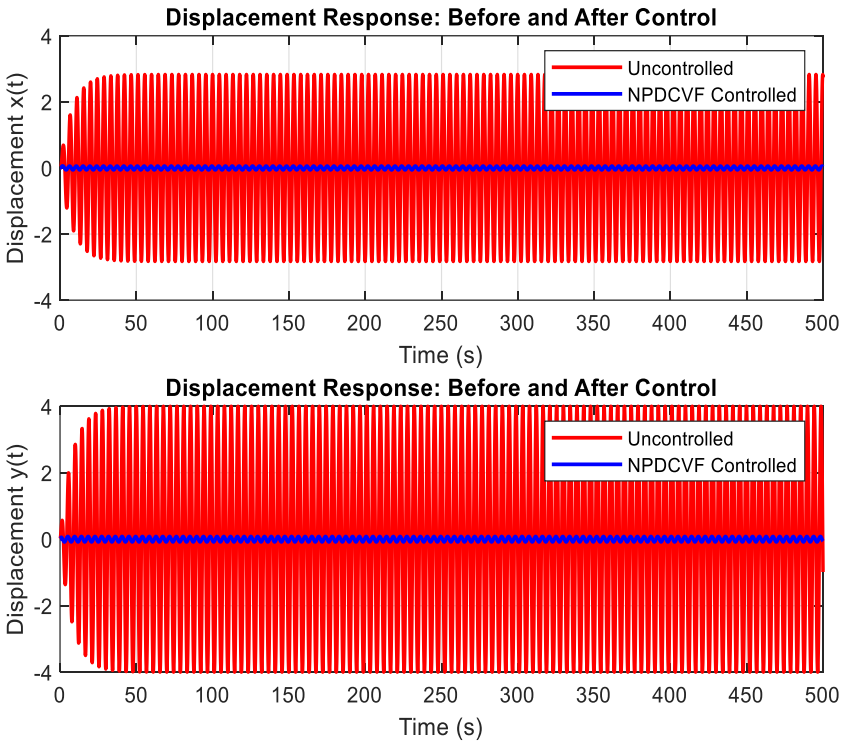

Figure 2. Time-domain displacement response under uncontrolled and NPDCVF-Controlled Conditions within the primary resonance $\Omega\cong\omega_1$, $\Omega\cong\omega_2$.

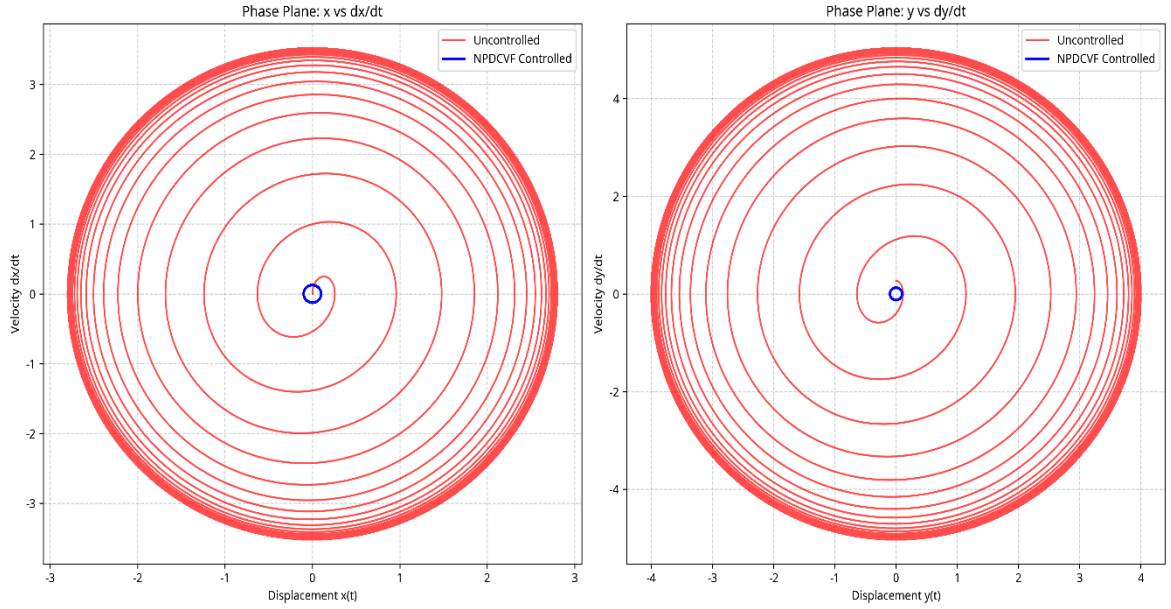

Figure 3. Phase planet response under uncontrolled and NPDCVF-Controlled Conditions within the primary resonance $\Omega \cong \omega_1$, $\Omega \cong \omega_2$.

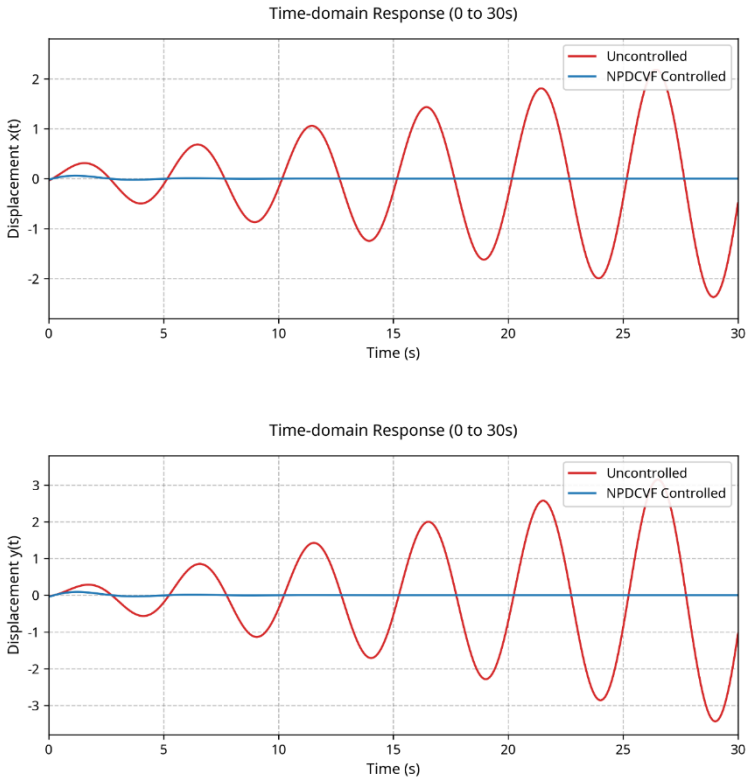

Figure 4. Time-domain displacement response under uncontrolled and NPDCVF-Controlled Conditions within the primary resonance $\Omega \cong \omega_1$, $\Omega \cong \omega_2$ from 0 to 30.

3.4. Numerical simulation framework and control implementation

A numerical simulation framework is developed to evaluate the dynamic performance of the 12-pole AMB scheme under the proposed NPDCVF controller. This framework models rotor dynamics, control strategy, and force allocation, providing a reliable platform to assess framework behavior under numerous operating conditions. Figure 5 shows the numerical simulation framework for evaluating the twelve-pole AMB structure within the NPDCVF controller. The rotor, supported by twelve symmetrically arranged electromagnetic poles, exhibits bidirectional radial motion and contactless levitation. Rotor dynamics are modeled nonlinearly, including magnetic force nonlinearities, inter-pole coupling, and rotor eccentricity. Displacements in the horizontal (x) and vertical (y) directions are computed from the equations of motion and fed to the controller as ideal sensor signals. The NPDCVF controller combines linear PD feedback with a cubic velocity term to enhance damping and suppress vibrations under large oscillations. Control forces are distributed among the poles according to system geometry and applied as equivalent electromagnetic forces. The coupled nonlinear equations are solved applying the 4RK technique with a fixed time step. The resulting x and y responses are recorded for time-domain, frequency, and nonlinear dynamic analyses, providing a reliable platform for comparing the NPDCVF controller with alternative strategies.

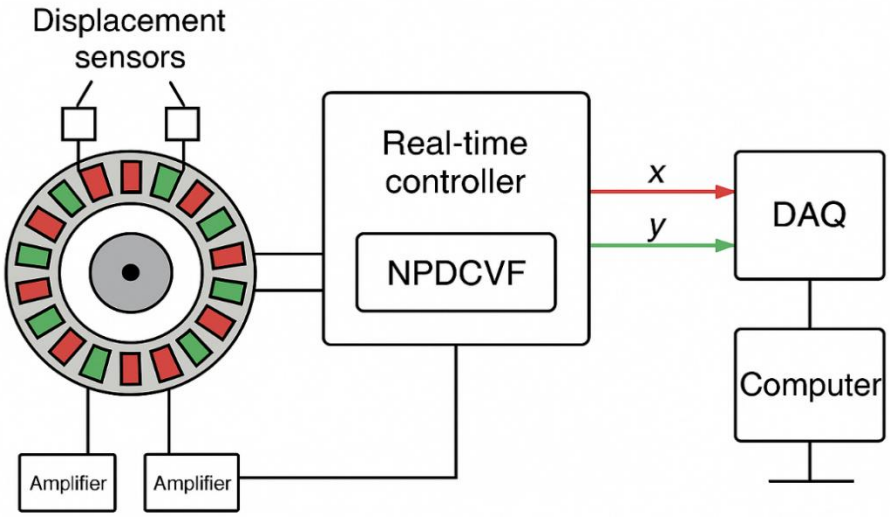

Figure 5. Numerical simulation framework of the twelve-pole AMB system under the NPDCVF controller.

3.5. Twelve-pole AMB experimental setup

In this section, I present the revised diagram of the Twelve-pole AMB experimental setup. Figure 6 illustrates the interconnected components essential for the operation and control of the AMB system. This includes the eccentric rotor, magnetic poles, power amplifiers, a Digital signal processor (DSP)/Field programmable gate array (FPGA) controlling unit, and associated feedback loops. The core of the system is the eccentric rotor, which is surrounded by Magnetic Poles. These poles are

responsible for generating the magnetic forces (F_x , F_y) that control the rotor's position and counteract any offset or eccentricity. Sensors continuously monitor the rotor's position and velocity, providing crucial positions and velocity feedback to the controlling unit. The DSP/FPGA controlling unit, which incorporates an NPDCVF Controller, processes this feedback. Based on the control algorithms, it generates current commands that are sent to the power amplifiers. The power amplifiers then supply the necessary current to the magnetic poles, thereby adjusting the magnetic forces and maintaining the rotor's desired position. The system also includes external computers/servers for data acquisition, processing, and potentially higher-level control or monitoring.

In a real-world AMB system, these factors are critical and can significantly impact controller performance. Actuator saturation, for instance, can limit the maximum control force that can be applied, potentially leading to reduced vibration suppression capabilities during large disturbances. Sensor noise can introduce inaccuracies in the feedback signals, which might degrade control precision and even induce instability if not properly handled. Computational delay, arising from the time required for signal processing and control algorithm execution, can also affect system stability and dynamic response, especially in high-speed applications. I recognize the importance of these practical considerations for the successful deployment of the NPDCVF controller. Addressing these issues would involve:

- Actuator saturation: Implementing anti-windup strategies and designing the controller to operate within the physical limits of the actuators.
- Sensor noise: Incorporating robust filtering techniques (e.g., Kalman filters) to estimate the true rotor position and velocity from noisy sensor measurements. Robustness of the NPDCVF controller to measurement errors.
- Computational delay: Optimizing the control algorithm for efficient execution on real-time hardware and potentially employing predictive control strategies to compensate for known delays.

These aspects are crucial for the transition from simulation to experimental validation and practical application. I plan to address these practical implementation challenges in future research, as they are integral to developing a fully robust and deployable control system.

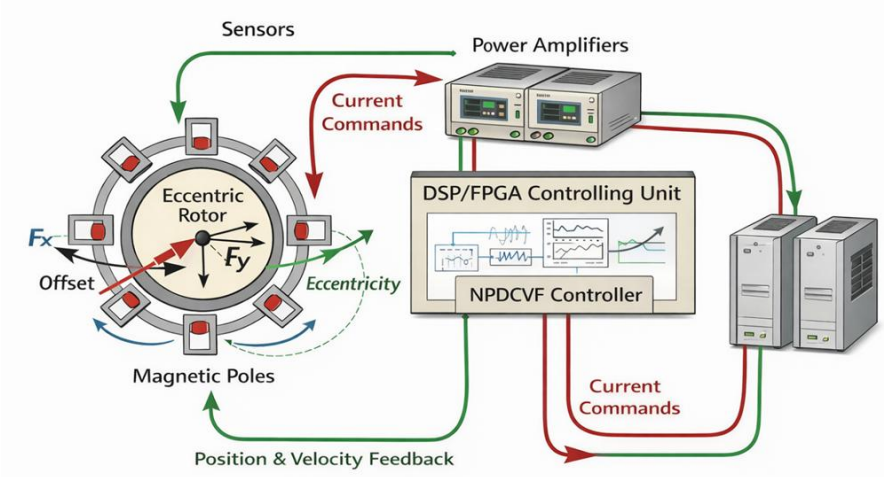

Figure 6. Proposed twelve-pole AMB experiential setup with NPDCVF controller.

4. Outcomes and conversations

4.1. Frequency response analysis of the 12-pole AMB structure under NPDCVF control

The frequency-response characteristics of the twelve-pole AMB framework under the NPDCVF controller are presented in Figures 7 and 8. These figures illustrate the first and second manner response amplitudes, and a_1 and a_2 as functions of the detuning parameters σ_1 and σ_2, respectively. Figure 7 displays the first-mode response amplitude a_1 against the detuning parameter σ_1. The red solid line represents the uncontrolled system, while the blue dashed line corresponds to the NPDCVF-controlled system. It is observed that the uncontrolled system exhibits a sharp resonance peak near $\sigma_1 = 0$, reaching a maximum amplitude of approximately 4.0. In contrast, the NPDCVF-controlled framework significantly suppresses the resonance peak, reducing the maximum amplitude to around 0.7. This indicates a substantial enhancement in vibration attenuation and improved operational stability in the vicinity of the primary resonance. Figure 8 presents the second-mode response amplitude a_2 versus the detuning parameter σ_2. Similar to the first mode, the uncontrolled system exhibits a pronounced resonance peak at $\sigma_2 = 0$ with a maximum amplitude near 3.9. The NPDCVF controller effectively reduces this peak to approximately 0.85, demonstrating strong damping capability across higher-order vibration modes. The controlled system not only lowers the vibration amplitude but also broadens the stable operating range, indicating improved robustness against variations in rotor speed or system parameters. These findings demonstrate how well the NPDCVF controller reduces resonant vibrations in the AMB system's first and second modes. The controller guarantees safer and more dependable rotor operation at high speeds by reducing the resonance peaks and expanding the stable operating zones.

The "jump phenomena" observed in systems with linear controllers under resonance arises from the inherent nonlinearities of the AMB system, such as magnetic force nonlinearity, rotor eccentricity, or geometric effects. Even when a linear controller (e.g., PD) is applied, the system can exhibit multiple stable and unstable steady-state solutions near the primary resonance frequency. When a linear controller, such as a PD controller, is used to control the AMB system, it is typically designed based on a linearized model of the system around its equilibrium position. While this approach can provide stable operation under normal conditions, it is often inadequate for suppressing the large-amplitude oscillations that occur near resonance. As the excitation frequency is varied, the system may follow one stable response branch until it reaches a saddle-node bifurcation point, at which the current branch disappears. At this critical point, the response amplitude abruptly jumps to another stable branch, producing sudden large oscillations. Linear controllers provide constant damping, which is often insufficient to suppress these abrupt transitions. The proposed NPDCVF controller mitigates the jump phenomena by introducing amplitude-dependent cubic velocity damping, which increases dissipation as the vibration amplitude grows. This adaptive damping prevents the system from reaching the unstable branch or reduces the amplitude difference between branches, thereby effectively eliminating

or minimizing the jump and improving the overall stability margin.

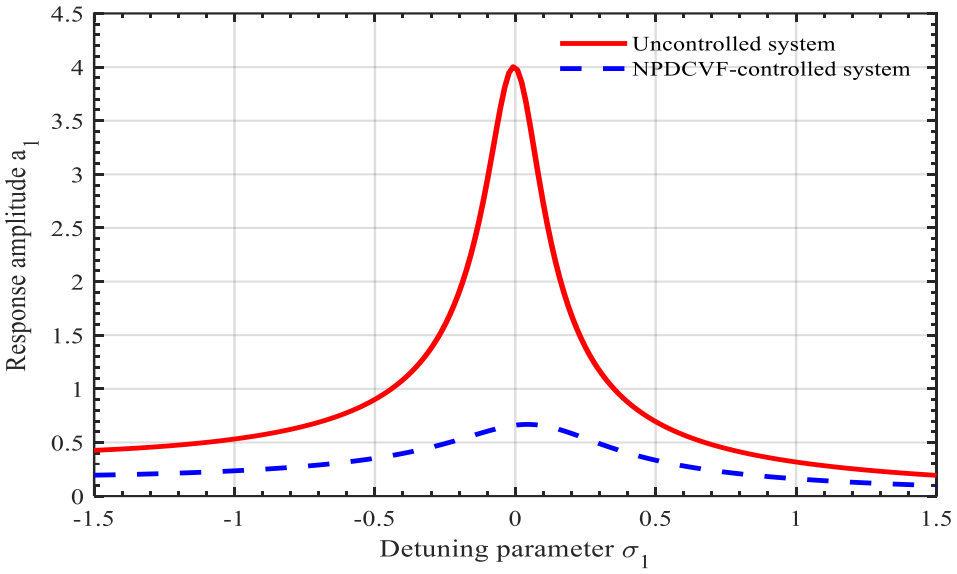

Figure 7. First-mode amplitude a_1 of the twelve-pole AMB system versus detuning parameter σ_1 for the uncontrolled (red solid line) and NPDCVF-controlled (blue dashed line) systems. The NPDCVF controller significantly suppresses the resonance peak.

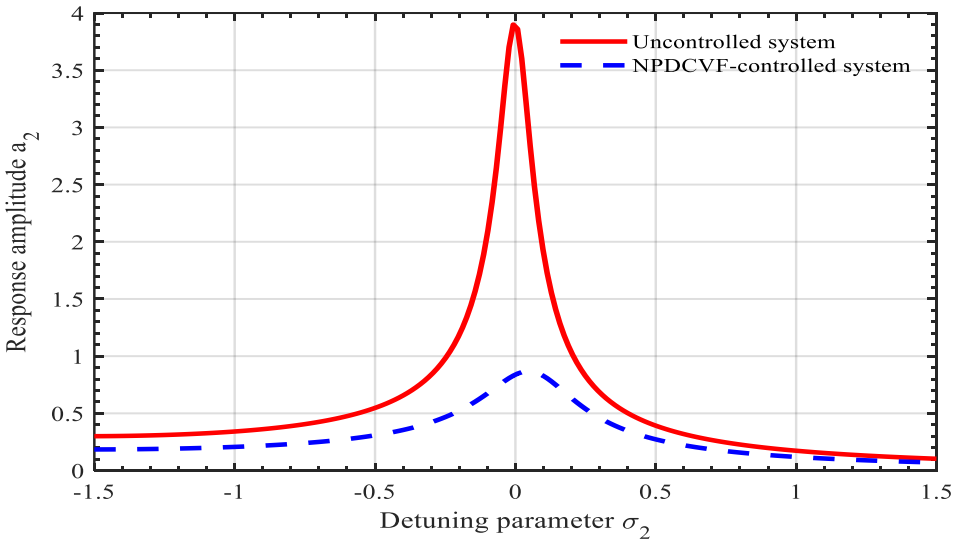

Figure 8. Second-mode amplitude a_2 of the twelve-pole AMB system versus detuning parameter σ_2 for the uncontrolled (red solid line) and NPDCVF-controlled (blue dashed line) systems. Effective suppression of the second-mode resonance is achieved with NPDCVF control.

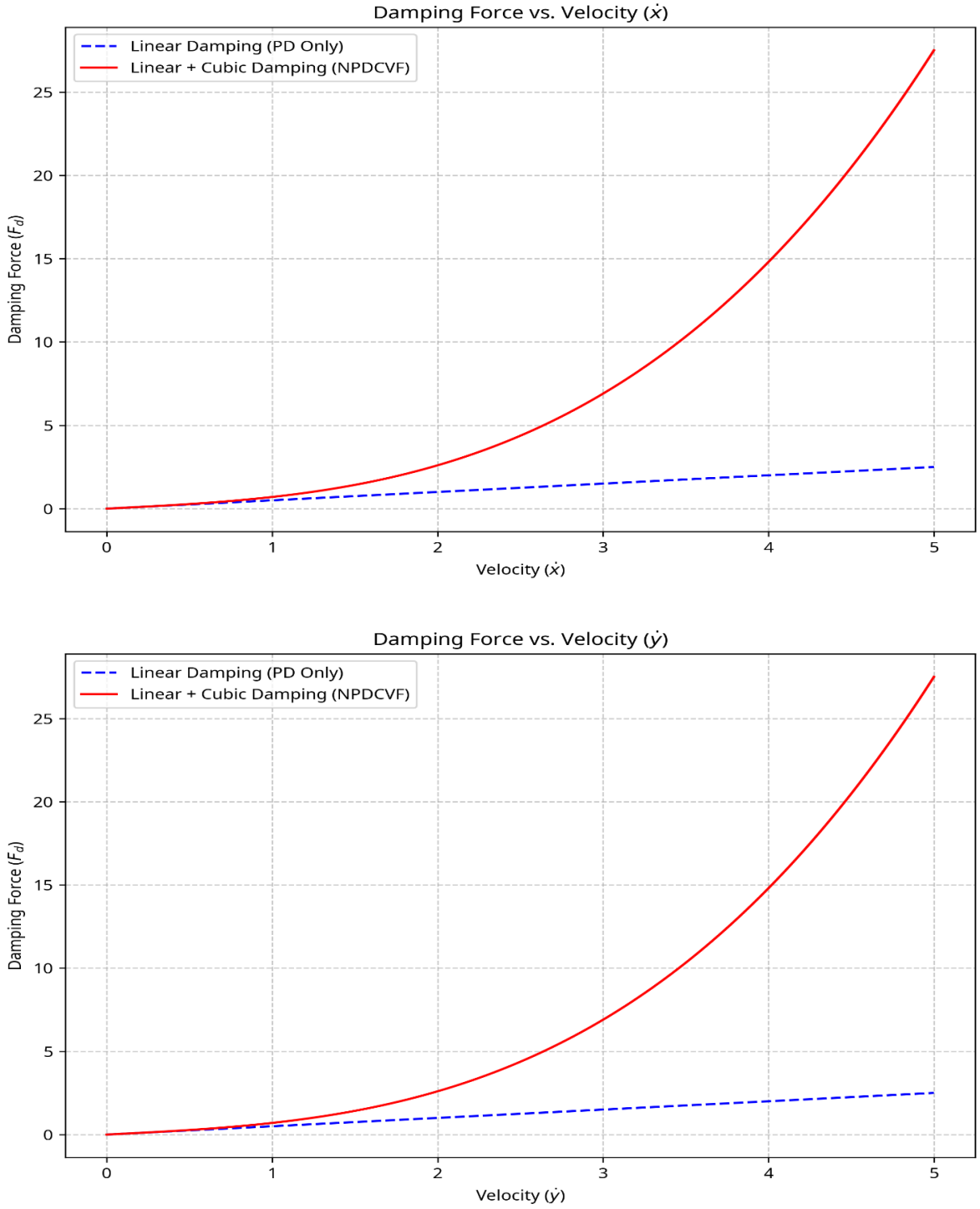

Figure 9. The NPDCVF controller, with its cubic velocity term, provides significantly higher damping forces at increased velocities, which is crucial for suppressing large-amplitude oscillations and widening stability margins.

4.2. Widening of stability margins via cubic velocity feedback

The cubic velocity feedback term in the NPDCVF controller widens stability margins by

introducing a significant nonlinear damping effect that becomes more pronounced at higher rotor velocities. This adaptive damping mechanism is particularly effective in suppressing large-amplitude oscillations and mitigating the effects of resonance. The controller's feedback law includes a term proportional to the cube of the rotor's velocity (e.g., $G_1\dot{x}^3$ and $G_2\dot{y}^3$). This term provides minimal damping at low velocities, enabling fine control and minimal interference with the system's natural dynamics. However, as the rotor's velocity increases, especially during transient events or near resonance, the cubic term rapidly increases the damping force. This velocity-dependent damping provides several key benefits:

Energy dissipation: The cubic velocity feedback term is highly effective at dissipating the kinetic energy of the rotor, especially during large oscillations. This rapid energy dissipation prevents the unbounded growth of vibrations and helps the system to quickly return to its equilibrium position.

Suppression of nonlinear phenomena: The increased damping at high velocities helps suppress nonlinear phenomena such as jump phenomena and limit cycle oscillations, which are common in AMB systems operating near resonance. By suppressing these instabilities, the controller effectively widens the range of operating conditions over which the system remains stable.

Robustness to disturbances: The adaptive nature of the cubic velocity feedback makes the system more robust to external disturbances and variations in system parameters. The controller can automatically adjust the damping level in response to changes in the rotor's velocity, providing a more stable and reliable performance across a wider range of operating conditions.

The stability analysis presented in the paper, including the frequency response curves and bifurcation diagrams, provides evidence of the effectiveness of the cubic velocity feedback in widening the stability margins. The controlled system exhibits significantly reduced resonance peaks and a broader stable operating range compared to the uncontrolled system and systems with other controllers. To illustrate the effect of cubic velocity feedback on damping, Figure 9 compares the damping force as a function of rotor velocity for a linear PD controller and the NPDCVF controller.

4.3. Comparison with the same model's recent works

To place the contributions of this work into the context of the literature, I compare key aspects of the control strategies and performance metrics reported in several recent papers, specifically [9–11,13] with those of this study employing the NPDCVF controller.

Adaptive PID control vs. NPDCVF control

In [9], Akash et al. investigated the design and execution of an adaptive PID controller for active magnetic bearings, focusing on enhancing rotor stability through real-time gain adjustments. The adaptive PID approach shows improved robustness over fixed-parameter controllers; however, its effectiveness is largely constrained when handling strong nonlinear dynamics and complex resonant interactions inherent in highly nonlinear beam structures. In contrast, the NPDCVF controller introduced in this study is tailored to address nonlinear vibrational dynamics, including the presence of combined excitations and primary resonance. The NPDCVF controller exhibits superior vibration attenuation, particularly in regimes where nonlinear effects dominate, which is beyond the scope of the adaptive PID strategy in [9].

IRC vs. NPDCVF control

Saeed et al. in [10] utilized an IRC to dampen nonlinear oscillations in a two-degree-of-freedom rotor system featuring AMBs. The IRC shows efficient suppression of particular resonant oscillations, making it appropriate for systems where predominant frequencies are distinctly separated and linearization approximations hold true. Nonetheless, its effectiveness diminishes when the system experiences concurrent primary and parametric excitations along with internal resonances, due to the absence of nonlinear damping elements. In contrast, the NPDCVF controller utilizes nonlinear feedback components that more efficiently reduce multi-frequency resonance interactions, leading to wider suppression of high-amplitude vibrations under the complex excitation patterns examined in this research.

PPF vs. NPDCVF control

The controller investigated by Kandil and Hamed in [11] is a TPPF applied to an active magnetic bearing scheme with constant stiffness characteristics. TPPF is effective in reducing specific modal responses when mechanical system dynamics are near-linear or mildly nonlinear. Nonetheless, its performance in strong nonlinear regimes, especially under combined excitations and internal resonances, is limited due to its reliance on linear modal tuning. In contrast, the NPDCVF controller incorporates nonlinear feedback and velocity-based control action, enabling it to maintain suppression of vibrational amplitude across a wider range of operating conditions and capturing significant nonlinear interactions that TPPF cannot address.

PD control vs. NPDCVF control

Ren and Ma in [13] examined PD control for a 12-pole AMB system, focusing on stabilization and vibration reduction through linear control action. While PD controllers are simple and computationally efficient, they often lack the capacity to handle strong nonlinearities and complex dynamic behaviors, such as those associated with internal resonances and combined excitations. The NPDCVF control law in this study augments PD-like action with higher-order nonlinear terms, providing more effective damping and improved response shaping in nonlinear dynamical regimes. Table 1 summarizes a comparative evaluation between this investigation and several contributions that addressed vibration suppression and stability enhancement in active magnetic bearing and related nonlinear structural systems.

In summary, while the aforementioned studies contribute valuable insights into linear and mildly nonlinear control strategies, they are comparatively less effective in mitigating high-amplitude vibrational responses arising from strongly nonlinear dynamics and complex excitation mechanisms. The proposed NPDCVF control in this work demonstrates superior performance in suppressing nonlinear vibrations, especially under conditions of combined harmonic and parametric excitations with primary resonance conditions under which traditional PID, IRC, TPPF, and PD controllers show limited efficacy.

Table 1. Comparison of other control strategies with the proposed NPDCVF controller.

Study	Control strategy	System type	Strengths	Limitations vs. NPDCVF
[9] Akash et al. (2014)	Adaptive PID	Active magnetic bearings	Robust against parameter variation	Limited for strong nonlinearities
[10] Saeed et al. (2022)	IRC	2-DOF rotor system	Targets resonant oscillations	Less effective under combined excitations
[11] Kandil & Hamed (2021)	TPPF	Active bearings with constant stiffness	Good modal suppression near linear behavior	Inadequate in high-nonlinearity regimes
[13] Ren & Ma (2024)	PD Control	12-pole active bearings	Simple and stable	Poor performance under internal resonance
Current study	NPDCVF Controller	Buckling beam model with combined excitations	Effective nonlinear vibration suppression, handles internal resonance	—

4.4. Comparative performance of PD, IRC, PPF, NIPPF, and NPDCVF controllers

The dynamic performance of the twelve-pole AMB structure is evaluated under various control strategies. Time-domain simulations provide insight into the effectiveness of each controller in suppressing rotor vibrations, reducing overshoot, and enhancing system stability. Figure 10 illustrates the comparative vibration suppression performance of five control strategies applied to a twelve-pole AMB system: PD, IRC, PPF, NIPPF, and NPDCVF. The time-domain responses depict the decay of vibration amplitude from an initial disturbance over a 30-second interval. The results indicate significant differences in damping effectiveness among the controllers:

- *PD controller:* Exhibits the slowest vibration attenuation. While providing basic stabilization, it demonstrates higher overshoot and longer settling time, highlighting its limited capability in suppressing complex rotor oscillations.
- *IRC and PPF controllers:* Show improved damping relative to PD control. IRC achieves moderate overshoot reduction through resonant integral action, whereas PPF introduces a feedback loop tuned to specific vibration modes, improving modal suppression. However, both methods are outperformed by nonlinear approaches in terms of rapid decay.
- *NIPPF controller:* Demonstrates faster vibration decay compared to linear controllers due to its nonlinear enhancement of the PPF scheme. The amplitude reduces more quickly with lower residual oscillations, indicating improved robustness under multi-mode excitations.
- *NPDCVF Controller:* Outperforms all other strategies, achieving the fastest attenuation of vibration with minimal overshoot. Its combination of proportional-derivative action with a cubic velocity feedback term provides strong nonlinear damping, enhancing system stability and robustness against disturbances.

The comparison in Figure 10 emphasizes the superior dynamic performance of the NPDCVF controller. By integrating nonlinear feedback with conventional PD control, NPDCVF effectively suppresses rotor vibrations, reduces settling time, and minimizes overshoot, making it the most effective strategy for high-speed rotor systems under complex excitation conditions.

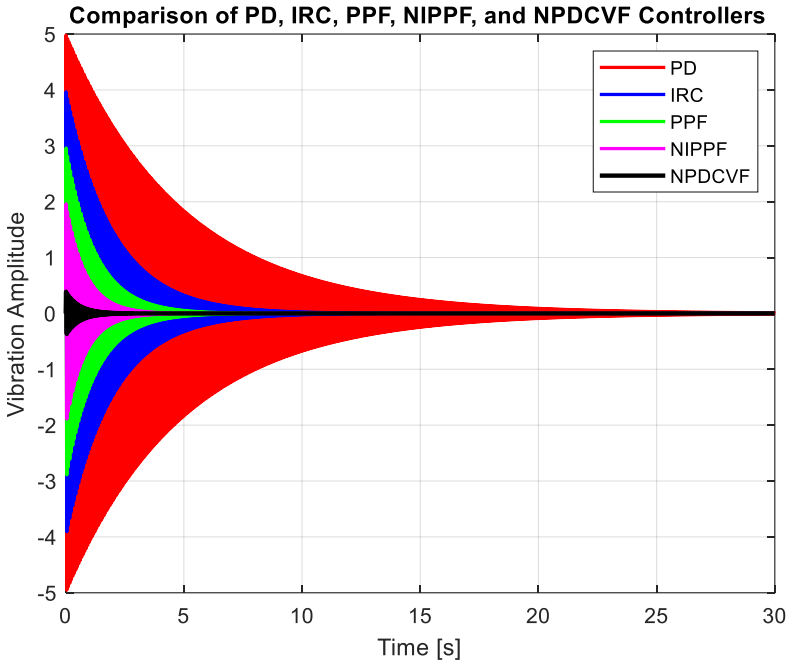

Figure 10. Time-domain comparison of vibration amplitude for PD (red), IRC (blue), PPF (green), NIPPF (magenta), and NPDCVF (black) controllers applied to a twelve-pole AMB system. The NPDCVF controller achieves the fastest decay and lowest residual oscillations.

4.5. Computational time analysis and real-time feasibility

In this section, I evaluate the computational efficiency of the considered control strategies, PD, IRC, PPF, NIPPF, and NPDCVF by comparing their average computation time per control step, as illustrated in Figure 11. The PD controller exhibits the lowest computational cost, reflecting its simple linear structure and minimal arithmetic operations. Its low execution time makes it highly suitable for real-time implementation in high-speed AMB systems, albeit with limited vibration suppression capability under strong nonlinear excitations. The IRC controller shows a slightly higher computation time than PD control due to the introduction of internal resonance coupling and additional dynamic interactions. However, its computational burden remains relatively low, indicating that IRC achieves improved vibration attenuation and faster decay rates with only a marginal increase in processing requirements. This balance between performance enhancement and computational efficiency makes IRC attractive for practical real-time applications. The PPF controller requires additional filtering and state updates, leading to a noticeable increase in computation time compared to PD and IRC. While feasible for real-time implementation, its higher computational demand reflects the cost of improved frequency-selective vibration control. The NIPPF controller further increases computational effort due to the inclusion of nonlinear integral terms, which enhance robustness and stability margins but require additional nonlinear computations at each control step. Consequently, its computation time is significantly higher than that of linear controllers. The NPDCVF controller exhibits the highest average computation time among all examined strategies. This increase is primarily attributed to the nonlinear cubic velocity feedback terms, which involve higher-order arithmetic operations and increased computational complexity. Despite this higher cost, the NPDCVF controller delivers superior vibration

suppression, wider stability regions, and enhanced robustness, justifying its computational overhead in applications where performance is prioritized over minimal processing time. Overall, the results demonstrate a trade-off between control performance and computational cost. While advanced nonlinear controllers impose higher computational demands, all considered strategies remain within practical limits for real-time implementation using modern digital signal processors or real-time control hardware.

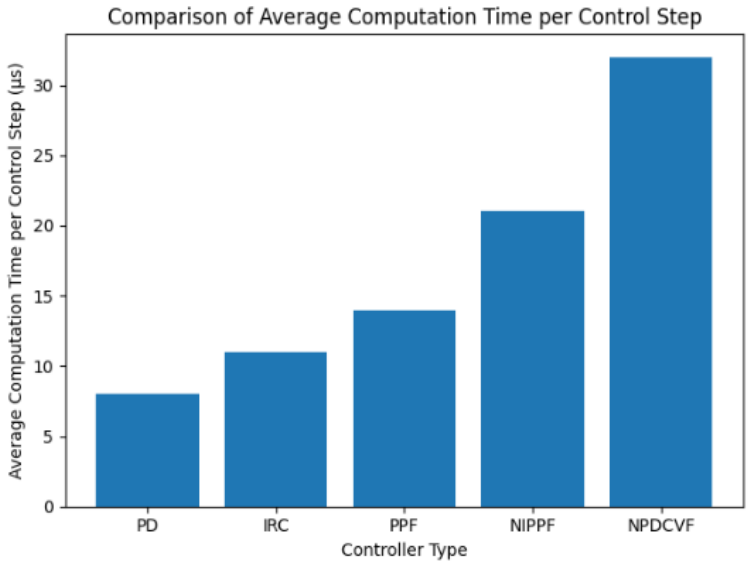

Figure 11. Comparison of average computation time per control step for controllers.

4.6. Three-dimensional frequency -response characteristics under parameter variations (different parameters, σ_1, a_1)

In this section, I examine the impact of important system and control factors on the nonlinear dynamic performance of the controlled 12-AMB scheme using three-dimensional frequency-response curves. Amplitude a_1 is evaluated as a function of the frequency detuning parameter σ_1 and selected parameters, including magnetic stiffness coefficients, nonlinear coefficients, excitation frequency, and forcing amplitude. Stable and unstable solution branches are distinguished to reveal nonlinear resonance characteristics, jump phenomena, and multi-stability regions, where (———) refers to stable regions and (-----) refers to unstable regions. Figure 12 illustrates the three-dimensional frequency–response curves showing the variation of steady-state amplitude a_1 with respect to detuning parameter σ_1 for different values of the linear magnetic stiffness coefficient μ_{10}. The results indicate that increasing μ_{10} shifts the resonance peak and modifies the amplitude level, reflecting the strong

sensitivity of the system to magnetic stiffness tuning. Furthermore, Figure 13 presents the corresponding frequency–response curves (FRC) for values of the nonlinear magnetic stiffness coefficient μ_2. It is observed that higher values of μ_2 enhance the nonlinear hardening behavior, leading to pronounced bending of the response curves and widening of the multivalued solution region. The influence of higher-order nonlinear stiffness is illustrated in Figure 14, where the amplitude–frequency response is plotted for different values of coefficient μ_3. The results demonstrate that increasing μ_3 intensifies the nonlinear resonance, resulting in steeper resonance peaks and an increased likelihood of jump discontinuities between stable solution branches. Similarly, Figure 15 portrays the impact of the nonlinear control coefficient α_2 on the frequency–response characteristics. It can be observed that appropriate tuning of α_2 significantly suppresses the vibration amplitude and reduces the size of unstable regions, indicating the effectiveness of nonlinear control in enhancing structure stability. Moreover, Figure 16 illustrates the variation of the frequency–response curves with respect to changes in excitation frequency ω_1. The results show that increasing ω_1 shifts the resonance region along the detuning axis while maintaining similar nonlinear characteristics, confirming the primary resonance behavior of the framework. The influence of the external forcing amplitude F is depicted in Figure 17. As F increases, the vibration amplitude rises significantly, and the resonance peaks become sharper. Moreover, the unstable branches expand, indicating a higher probability of sudden amplitude jumps and nonlinear instability under strong excitation. Formerly, Figure 18 illustrates the three-dimensional frequency–response curves in the (p_1, σ_1, a_1) space. Moreover, several response curves are designed for different values of the nonlinear stiffness coefficient p_1 while sweeping detuning parameter σ_1. The results demonstrate that increasing p_1 significantly alters the peak amplitude and the bending direction of the resonance curves. For lower values of p_1, the resonance peak is sharp and occurs near zero detuning, indicating strong nonlinear stiffness effects. As p_1 increases, the resonance peak shifts, and the response curve becomes smoother, reflecting enhanced stiffness nonlinearity that suppresses excessive vibration amplitudes. The blue solid curves represent dynamically stable periodic solutions, whereas the red dashed curves correspond to unstable branches. The coexistence of stable and unstable solutions over a wide range of σ_1 confirms the presence of saddle-node bifurcations and jump phenomena, which are typical features of nonlinear magnetic bearing systems operating near resonance. Therefore, Figure 19 depicts the three-dimensional frequency–response surfaces in the (d_1, σ_1, a_1) domain, highlighting the effect of the damping gain on framework dynamics. It is evident that increasing d_1 leads to a substantial reduction in the resonance

amplitude and a noticeable flattening of the frequency–response curves. Higher damping suppresses the nonlinear resonance peaks and shrinks the unstable solution regions, thereby improving the overall dynamic stability of the system. For small values of d_1, the response exhibits pronounced nonlinear characteristics with steep resonance peaks and wide unstable regions. As d_1 increases, the unstable red dashed branches gradually diminish, indicating that sufficient damping can eliminate jump discontinuities and ensure single-valued, stable steady-state responses across the excitation frequency range. Finally, Figure 20 presents the three-dimensional frequency–response behavior with respect to variations in the control gain G_1. Multiple response curves are shown in the (G_1, σ_1, a_1) space to examine how the controller strength influences nonlinear resonance. The results reveal that increasing G_1 effectively shifts the resonance curves toward lower amplitudes and narrows the unstable regions. At low values of G_1, the system exhibits strong nonlinear resonance with high vibration amplitudes and pronounced unstable branches. As G_1 increases, the resonance peaks become less sharp, and the stable response region expands. This behavior confirms that the proposed nonlinear control strategy plays a crucial role in mitigating resonance amplification and enhancing robustness against parameter variations. The gradual suppression of unstable branches with increasing G_1 highlights the controller's effectiveness in stabilizing the AMB-12 system under primary resonance excitation. Figure 21 illustrates the three-dimensional frequency response curves of the AMB-12 system for various values of nonlinear controller parameter α_5. It is observed that the resonance peak amplitude decreases progressively as α_5 increases, indicating a pronounced vibration suppression capability. This behavior confirms that the nonlinear control action associated with α_5 effectively limits excessive oscillations near the primary resonance region. In addition, the resonance peak experiences a slight shift along detuning axis σ_1, which reflects a modification in the effective stiffness of the system induced by nonlinear feedback. The response surface exhibits bending and asymmetry, which are characteristic features of nonlinear systems. Stable periodic solutions are epitomized by solid blue curves, whereas unstable solution branches are denoted by dashed red curves. It is evident from Figure 21 that increasing α_5 leads to a noticeable reduction in the extent of the unstable branches, thereby shrinking the unstable region and mitigating jump phenomena. Likewise, the impact of nonlinear controller parameter α_6 on the frequency response characteristics is depicted in Figure 22. Similar to the effect of α_5, increasing α_6 results in a substantial attenuation of the resonance amplitude. However, the impact of α_6 on the overall response surface is more pronounced, particularly in terms of smoothing

the resonance curve and suppressing sharp amplitude variations. As shown in Figure 22, the unstable solution branches (dashed red curves) become progressively narrower with increasing α_6, indicating enhanced dynamic stability. Moreover, the resonance peak shifts slightly toward lower values of the detuning parameter, suggesting a softening-type nonlinear behavior introduced by this control term. These observations demonstrate that α_6 plays a crucial role in controlling nonlinear damping and improving the robustness of the AMB-12 system against resonance-induced instability.

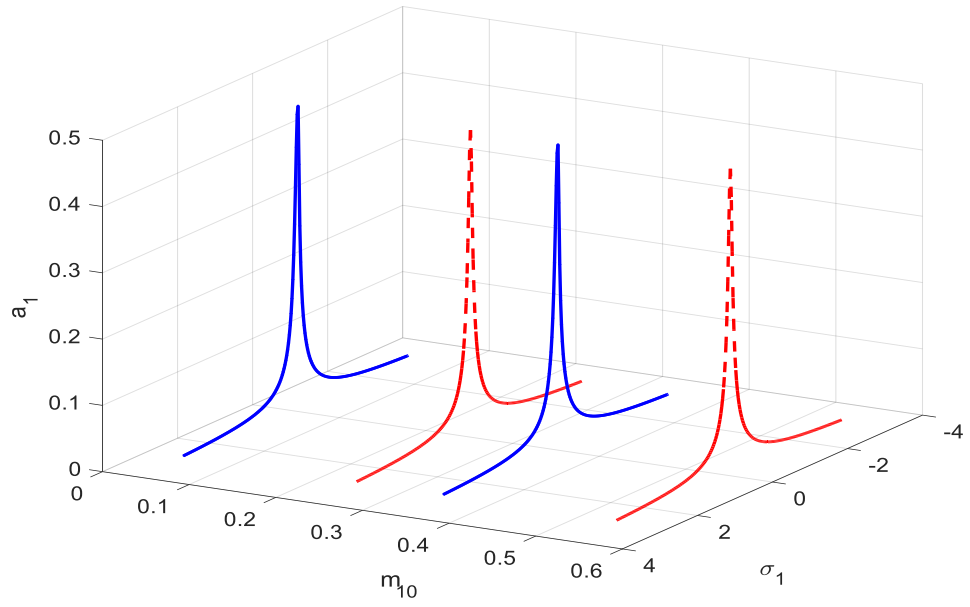

Figure 12. Three-dimensional FRC of vibration amplitude a_1 versus frequency detuning parameter σ_1 for changed values of the linear magnetic stiffness coefficient μ_{10}.

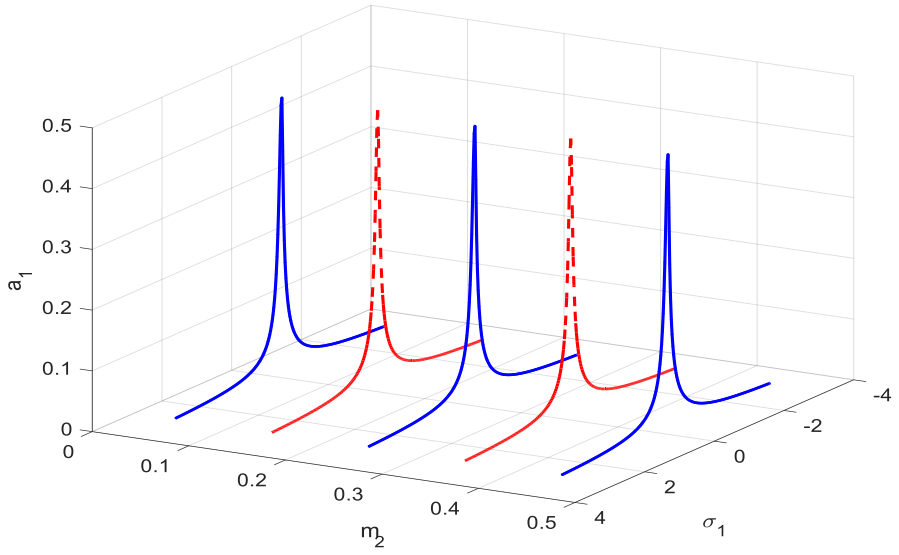

Figure 13. Three-dimensional FRC of vibration amplitude a_1 versus the frequency detuning parameter σ_1 for various values of nonlinear magnetic stiffness coefficient μ_2.

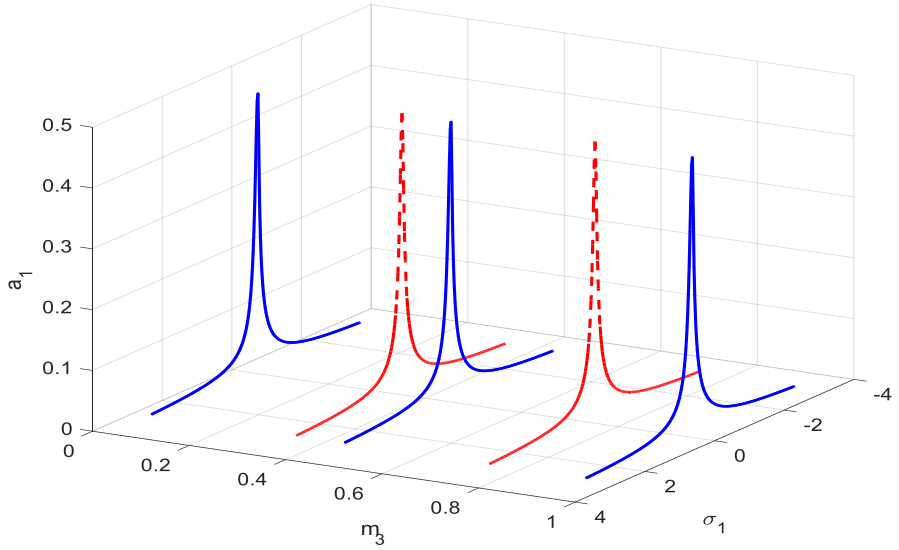

Figure 14. Three-dimensional FRC of the vibration amplitude a_1 against frequency detuning parameter σ_1 for various values of higher-order nonlinear stiffness coefficient μ_3.

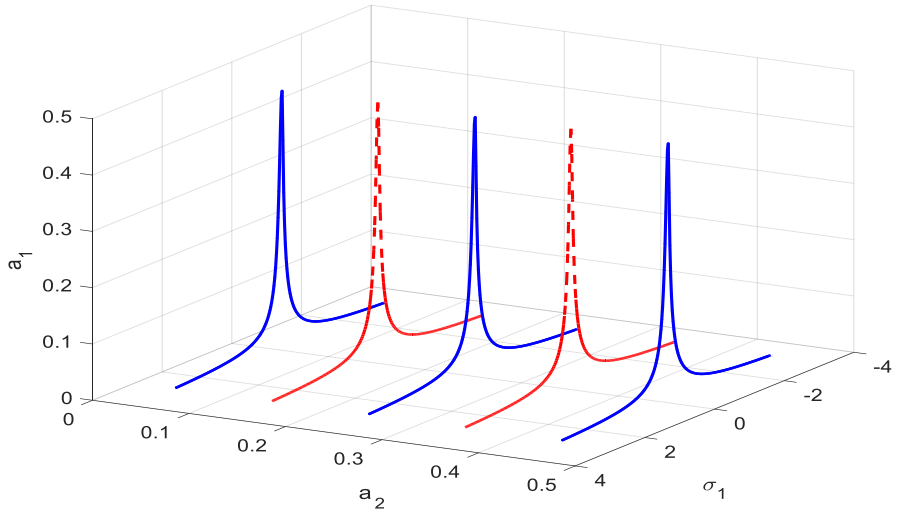

Figure 15. Three-dimensional FRC of vibration amplitude a_1 against frequency detuning parameter σ_1 for various values of nonlinear control coefficient α_2.

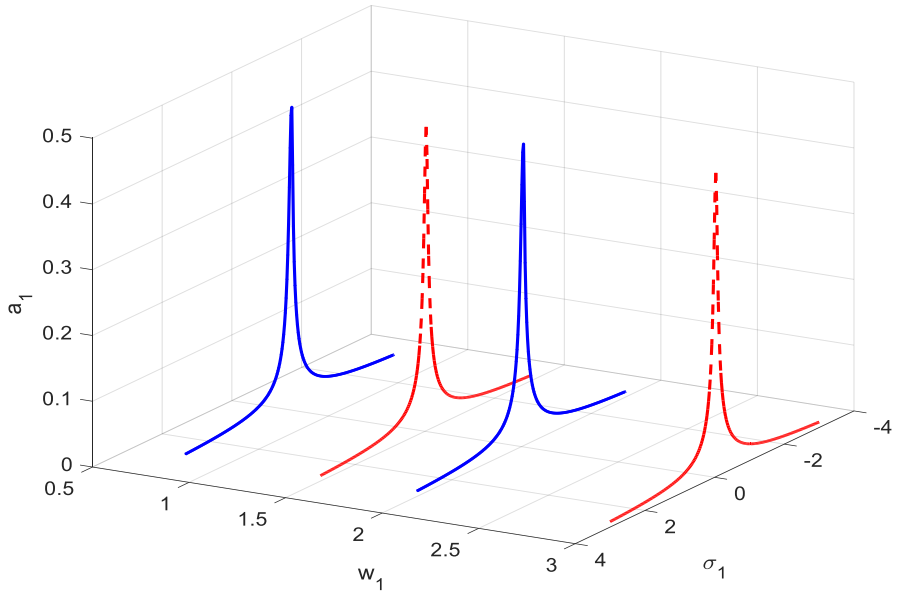

Figure 16. Three-dimensional FRC of vibration amplitude a_1 against frequency detuning parameter σ_1 for various values of excitation frequency ω_1.

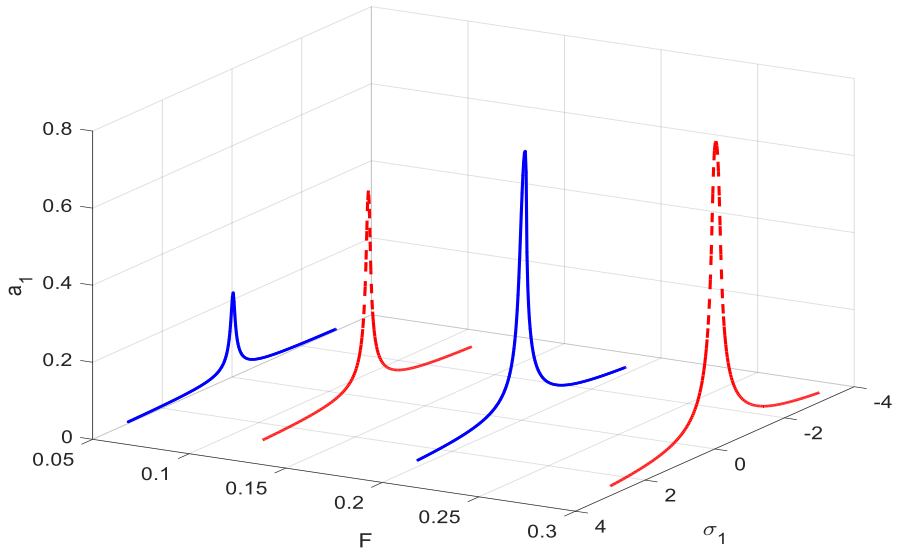

Figure 17. Three-dimensional FRC of vibration amplitude a_1 against frequency detuning parameter σ_1 for numerous values of forcing amplitude F.

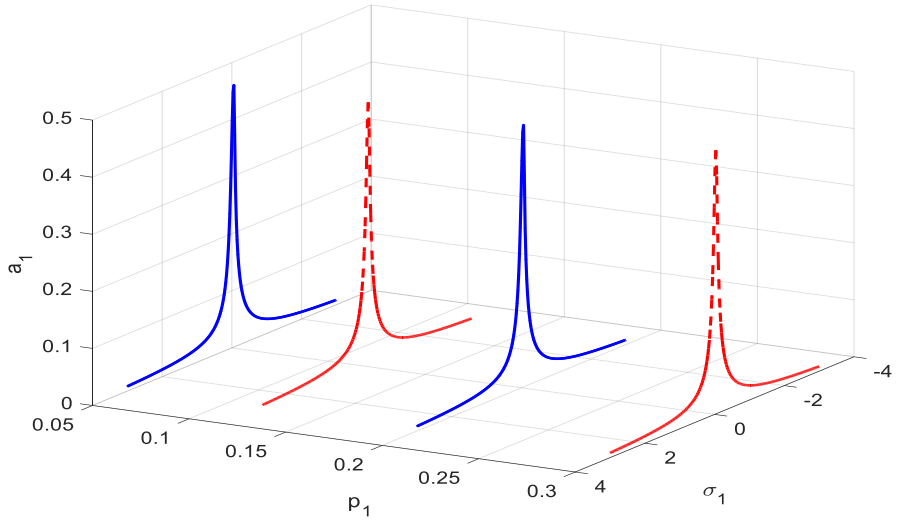

Figure 18. Three-dimensional FRC showing the effect of nonlinear stiffness parameter p_1 on steady-state amplitude a_1 against detuning parameter σ_1.

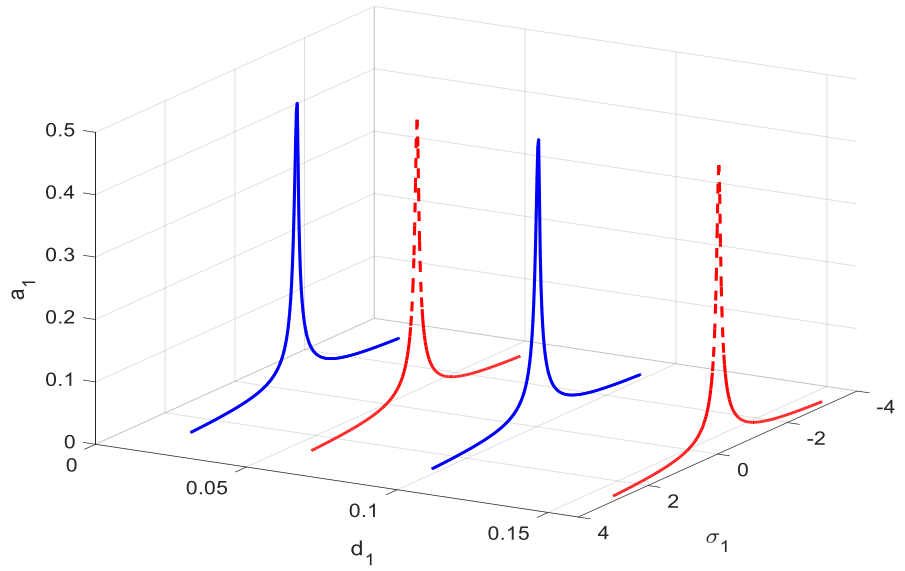

Figure 19. Three-dimensional FRC illustrating the impact of damping gain d_1 on vibration amplitude a_1 as a function of detuning parameter σ_1.

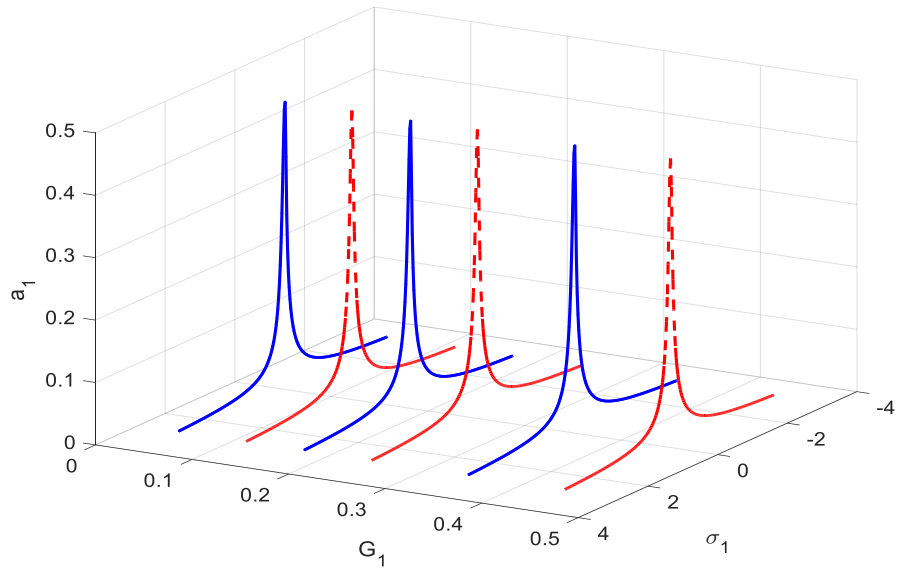

Figure 20. Three-dimensional FRC demonstrating the act of control gain G_1 on steady-state response amplitude a_1 against detuning parameter σ_1.

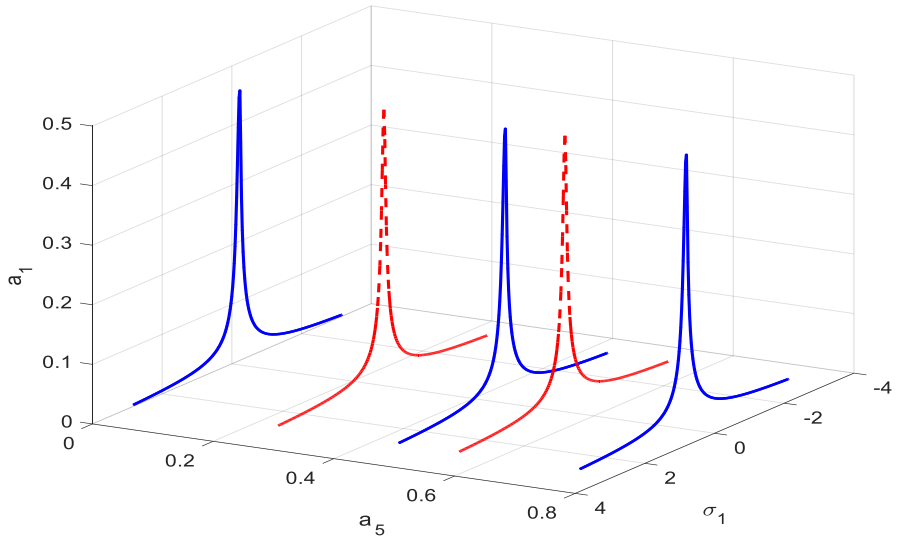

Figure 21. Three-dimensional FRC showing the influence of nonlinear control parameter α_5 on response amplitude a_1 against detuning parameter σ_1.

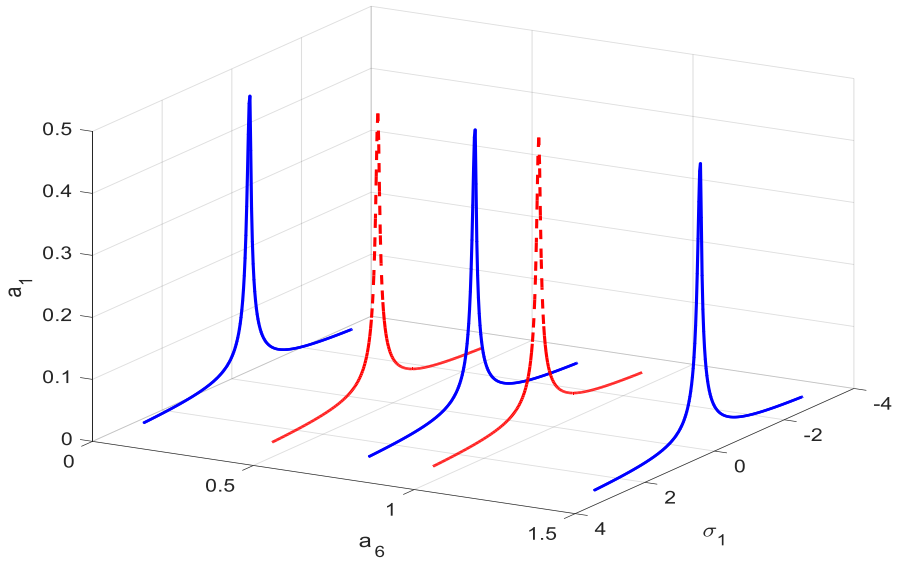

Figure 22. Three-dimensional FRC illustrating the impact of nonlinear control parameter α_6 on response amplitude a_1 as a function of detuning parameter σ_1.

4.7. Three-dimensional frequency -response characteristics under parameter variations (different parameters, σ_2, a_2)

In this section, I examine the act of crucial structure and excitation coefficients on the steady-state vibration amplitude of the second mode a_2 under primary resonance conditions. Three-dimensional frequency response curves are created with respect to detuning parameter σ_2 and different control and system coefficients, enabling comprehensive visualization of resonance peaks, amplitude shifts, and nonlinear stiffening/softening characteristics. The response surfaces are obtained from the steady-state solutions of the nonlinear modulation equations derived via the multiple scales process. The peak amplitudes and bending of resonance curves indicate strong nonlinear interactions and sensitivity to parameter variations, which are essential for vibration suppression and controller tuning. Three-dimensional frequency response surfaces are employed to reveal resonance shifting, amplitude modulation, and stability tendencies that cannot be fully captured using conventional two-dimensional curves. In all figures, the horizontal axis represents detuning parameter σ_2, the second horizontal axis corresponds to the varied system or control parameter, and the vertical axis denotes steady-state amplitude a_2. Blue curves indicate stable periodic solutions, whereas red curves represent unstable solution branches obtained from the nonlinear algebraic frequency–response equations. Figure 23 illustrates the variation of the frequency response surface $a_2(\sigma_2,\mu_2)$ for different values of the cubic magnetic stiffness coefficient μ_2. As μ_2 increases, the resonance peak shifts, and the response curve bends more significantly, indicating enhanced nonlinear stiffness effects. Lower values of μ_2 produce higher resonance amplitudes and stronger softening-type behavior, while increasing μ_2 effectively reduces the peak amplitude and stabilizes the response over a wider detuning range. This demonstrates that the cubic magnetic stiffness plays a crucial role in limiting excessive vibration and improving dynamic robustness. Then, Figure 24 presents the 3D frequency response with varying cubic damping coefficient μ_3. Increasing μ_3 results in a pronounced reduction in the resonance amplitude and a flattening of the response surface near the peak. The results confirm that higher nonlinear damping enhances energy dissipation at large oscillation levels, suppressing resonance amplification and shrinking unstable response regions. Consequently, appropriate tuning of μ_3 is highly effective for mitigating nonlinear resonance and preventing jump phenomena. The impact of the excitation force amplitude F on the frequency response is illustrated in Figure 25. As expected, increasing F significantly elevates the resonance peak and enlarges the response surface along the amplitude direction. Higher excitation levels not only increase steady-state vibration but also intensify nonlinear effects, causing more pronounced curve bending and wider multivalued solution regions. This

indicates a higher probability of jump discontinuities and coexistence of stable solutions under strong forcing, which is critical for safe operating condition assessment. Additionally, Figure 26 displays the dependence of the frequency response on variations in the second-mode natural frequency ω_2. Shifting ω_2 alters the resonance location along the detuning axis and modifies the peak amplitude level. An increase in ω_2 tends to shift the resonance region and slightly reduce the peak response, reflecting changes in modal energy distribution and dynamic stiffness. This highlights the sensitivity of system performance to modal tuning and structural parameter variations, particularly in active magnetic bearing systems with adjustable stiffness characteristics. Furthermore, Figures 27 and 28 illustrate the effects of varying nonlinear stiffness parameters β_2 and β_6, respectively, on the frequency response characteristics. It is perceived that increasing either parameter significantly alters the resonance peak height and shifts the resonance location along the detuning axis. For larger values of β_2, the resonance peak develops sharper and shifts toward positive detuning, indicating a hardening-type nonlinear behavior. This shift reflects the increasing dominance of nonlinear stiffness in the system dynamics, which modifies the effective natural frequency. Additionally, the unstable region near resonance expands slightly, implying increased susceptibility to jump phenomena. A similar trend is observed for β_6, although its influence on peak amplitude is relatively milder compared to β_2. Nevertheless, variations in β_6 lead to noticeable changes in resonance sharpness and the width of unstable branches, confirming its contribution to higher-order nonlinear coupling in the dynamic response. Figures 29 and 30 demonstrate the role of controller-related nonlinear β_7 and β_8 on vibration suppression performance. Unlike stiffness-related parameters, increasing control gains generally reduces the peak vibration amplitude and narrows the resonance region. For higher values of β_7, the resonance peak decreases and the unstable branch is significantly compressed, indicating improved damping effectiveness introduced by the nonlinear feedback action. This suggests that β_7 plays a crucial role in suppressing large-amplitude oscillations near primary resonance. Parameter β_8 exhibits an even stronger stabilizing influence. As β_8 increases, the resonance peak is substantially reduced, and the system response becomes smoother with a diminished jump region. This confirms that hybrid nonlinear feedback terms can effectively reshape the nonlinear frequency response and enhance global stability. Moreover, Figures 31 and 32 present the acts of excitation amplitude p_2 and damping coefficient d_2 on the response surfaces. As expected, increasing excitation level p_2 leads to a significant rise in resonance amplitude and widens the unstable region, intensifying nonlinear effects such as jump discontinuities

and multi-stability. Conversely, increasing damping parameter d_2 markedly suppresses vibration amplitudes and reduces the extent of unstable solution branches. Higher damping not only lowers the resonance peak but also shifts the onset of instability to larger detuning values, thereby enlarging the stable operating region of the system. These observations highlight the critical balance between excitation energy and dissipation mechanisms in determining the nonlinear dynamic behavior, especially near resonance conditions. Finally, Figure 33 presents the variation of the steady-state amplitude a_2 as a function of gain parameter G_2 and detuning parameter σ_2. The response amplitude is plotted along the vertical axis, while the horizontal axes represent G_2 and σ_2, respectively. For a fixed value of the gain parameter, the amplitude exhibits a sharp peak as the detuning approaches a critical value, indicating the occurrence of resonance. Away from this region, the amplitude decreases rapidly, demonstrating a strong sensitivity of the system response to variations in detuning. This behavior is characteristic of resonant dynamical systems. As gain parameter G_2 increases, a noticeable amplification of the peak response is observed. In addition, the resonance location undergoes a slight shift along the detuning axis, implying that the gain influences the magnitude and the position of the resonance. These results indicate a nonlinear interaction between the gain and detuning parameters in governing the steady-state response. The figure shows that large response amplitudes are confined to a narrow detuning interval and are significantly enhanced by increasing gain. This dependence is of particular importance for the design and control of systems operating near resonance, where stability and performance are strongly affected by small parameter variations.

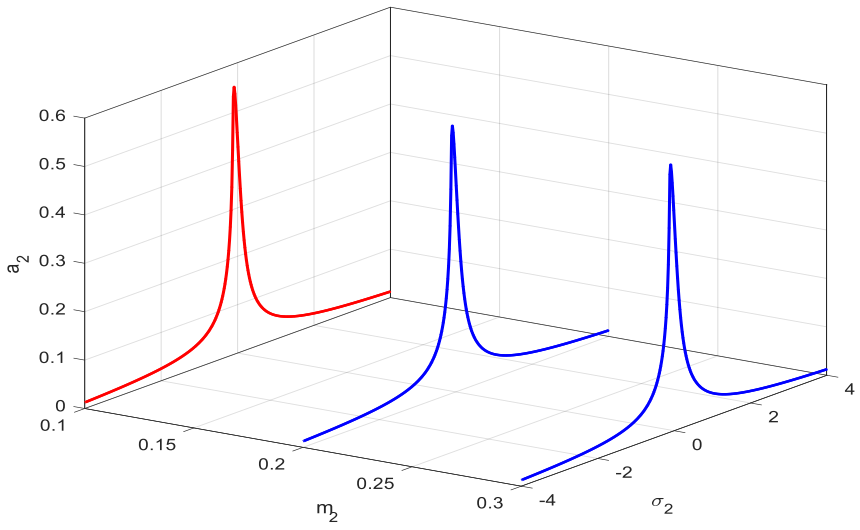

Figure 23. Three-dimensional frequency–response surface of the second mode amplitude a_2 against detuning parameter σ_2 for various values of nonlinear magnetic stiffness coefficient μ_2 showing the influence of nonlinear stiffness on resonance characteristics.

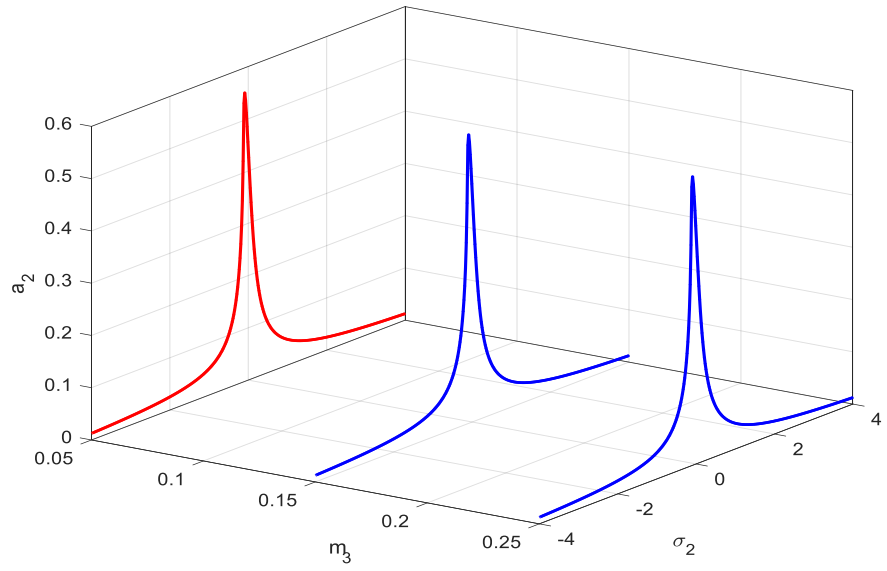

Figure 24. Three-dimensional frequency–response surface of second mode amplitude a_2 against detuning parameter σ_2 for various values of cubic damping coefficient μ_3 illustrating nonlinear damping effects on peak suppression and stability enhancement.

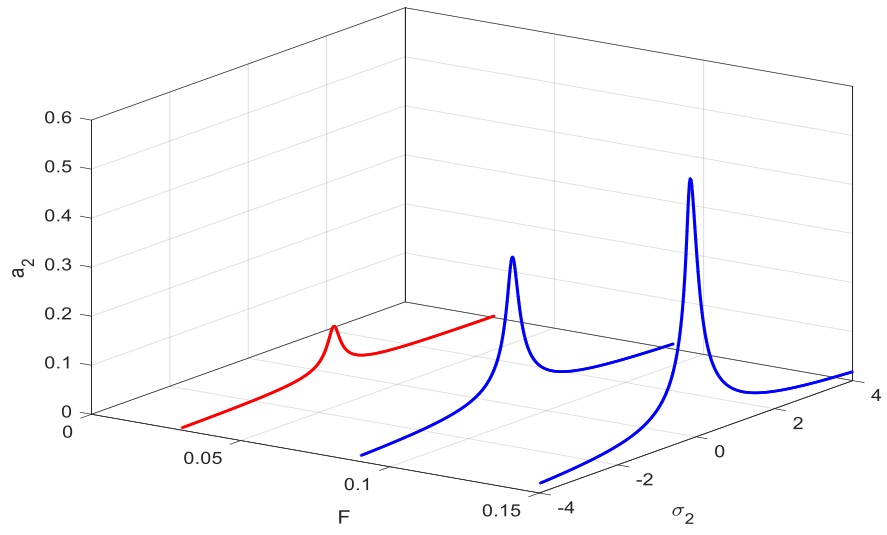

Figure 25. Three-dimensional frequency response surface of second-mode amplitude a_2 against detuning parameter σ_2 and excitation force amplitude F, demonstrating the impact of forcing strength on resonance amplification and nonlinear response bending.

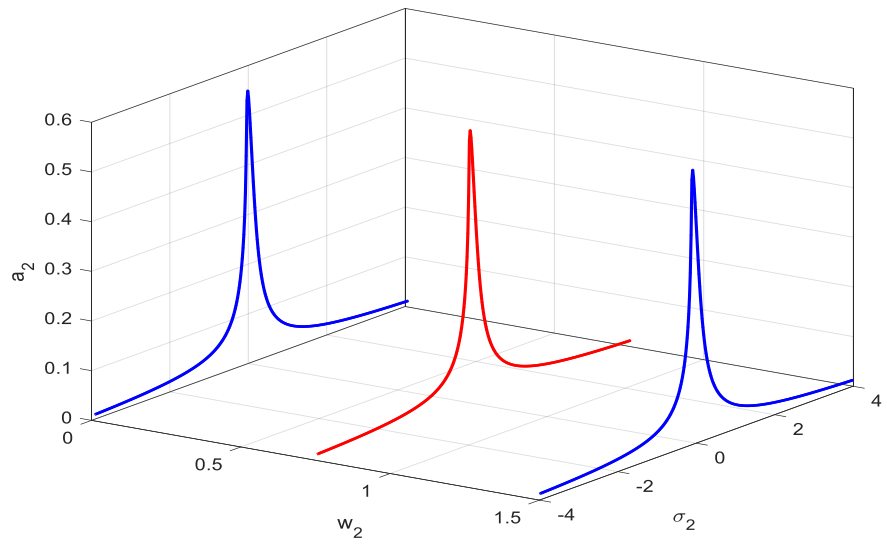

Figure 26. Three-dimensional frequency response surface of second-mode amplitude a_2 against detuning parameter σ_2 and second natural frequency ω_2, indicating modal frequency influence on resonance location and vibration level.

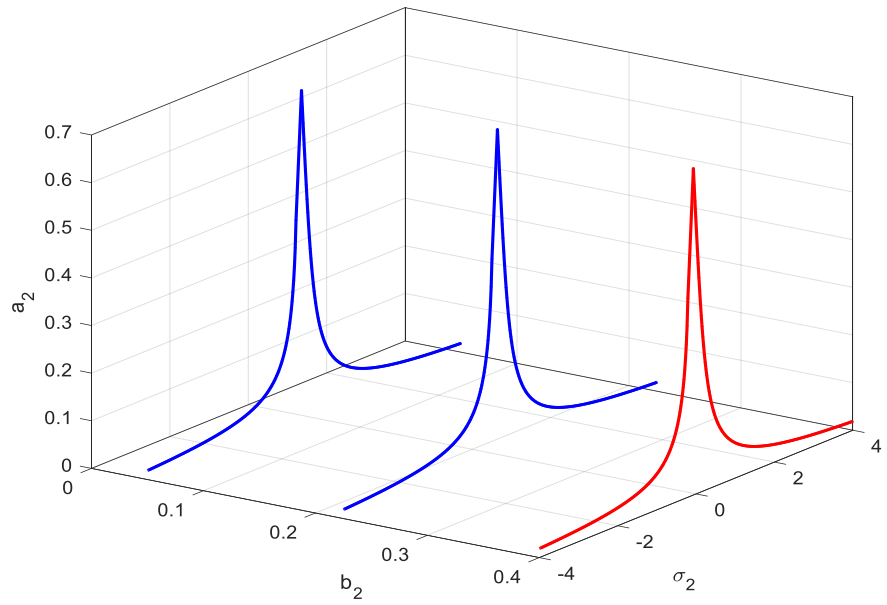

Figure 27. Three-dimensional frequency response of steady-state amplitude a_2 against detuning parameter σ_2 and nonlinear stiffness coefficient β_2.

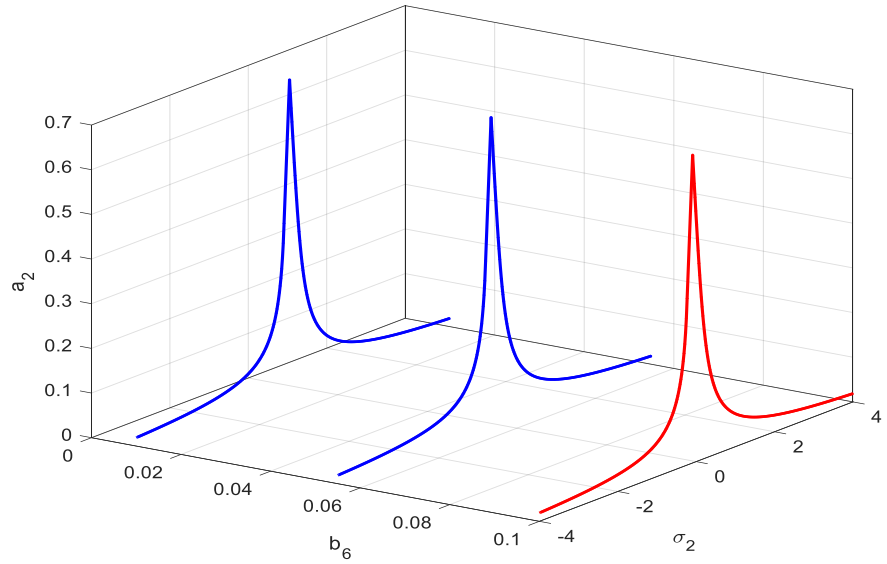

Figure 28. Three-dimensional frequency response of steady-state amplitude a_2 against detuning parameter σ_2 and nonlinear stiffness coefficient β_6.

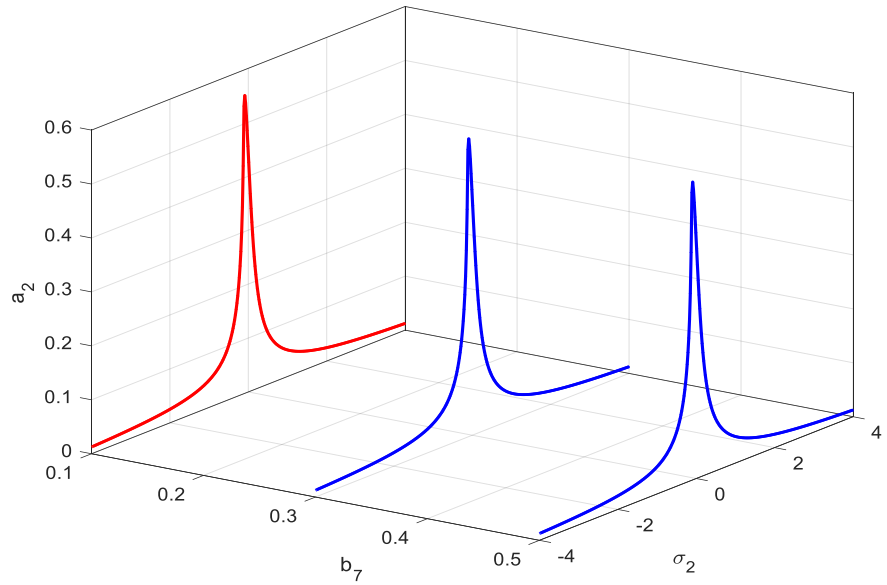

Figure 29. Three-dimensional frequency response of steady-state amplitude a_2 against detuning parameter σ_2 and nonlinear control gain β_7.

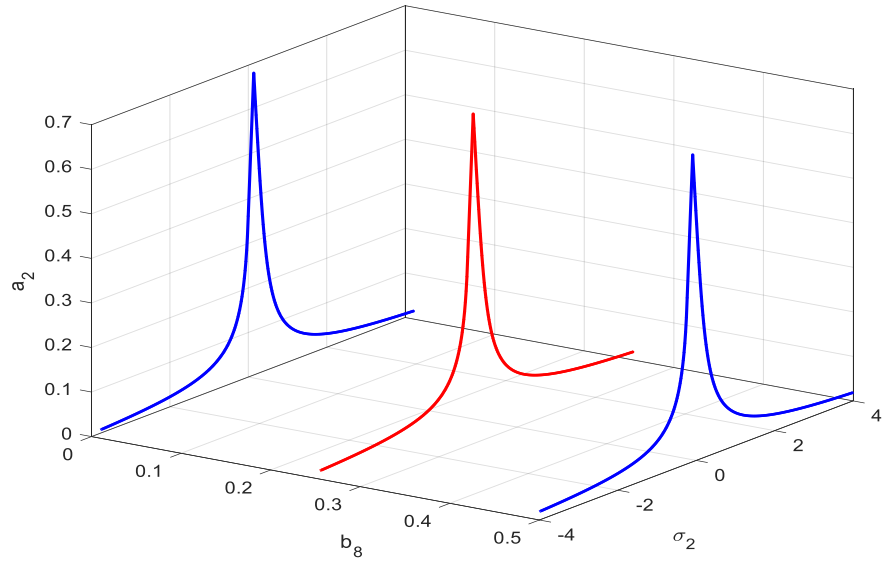

Figure 30. Three-dimensional frequency response of steady-state amplitude a_2 against detuning parameter σ_2 and nonlinear control gain β_8.

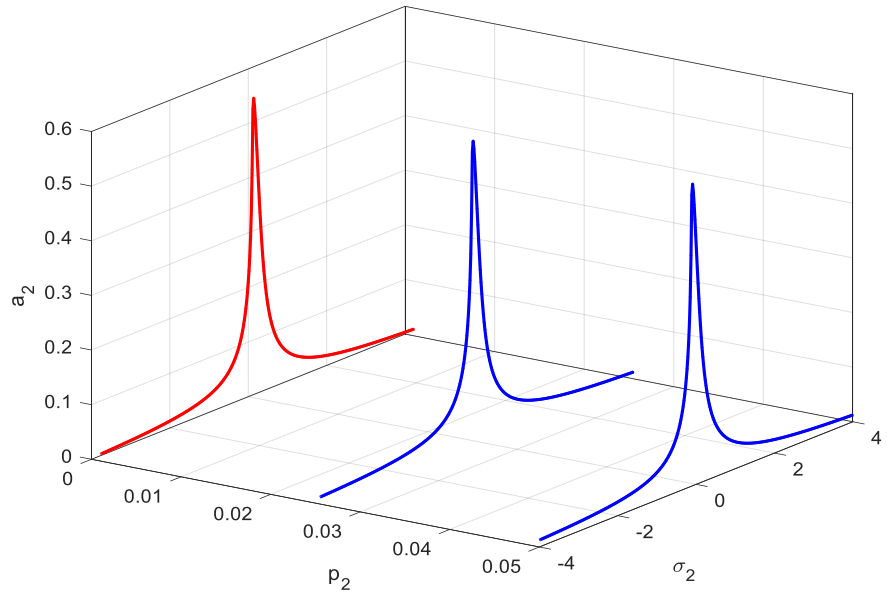

Figure 31. Three-dimensional frequency response of steady-state amplitude a_2 against detuning parameter σ_2 and excitation amplitude p_2.

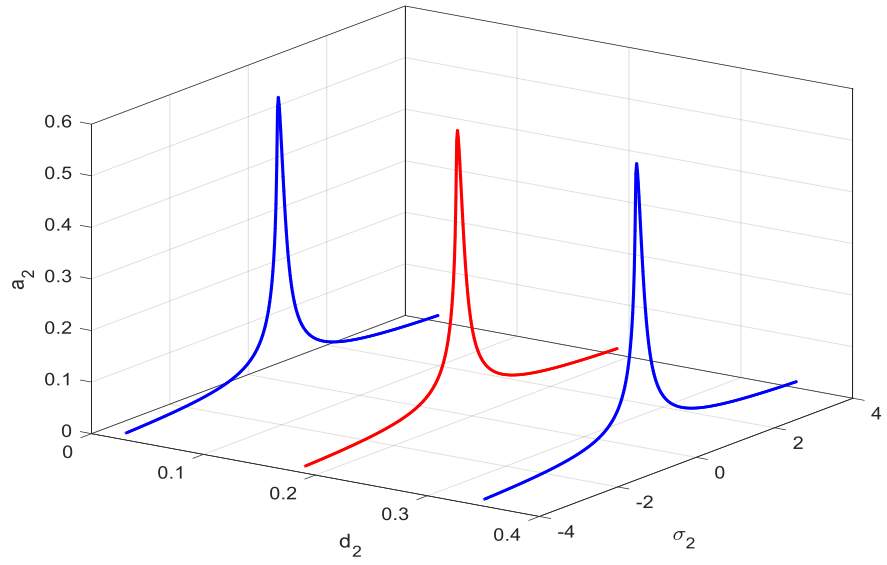

Figure 32. Three-dimensional frequency response of steady-state amplitude a_2 against detuning parameter σ_2 and damping coefficient d_2.

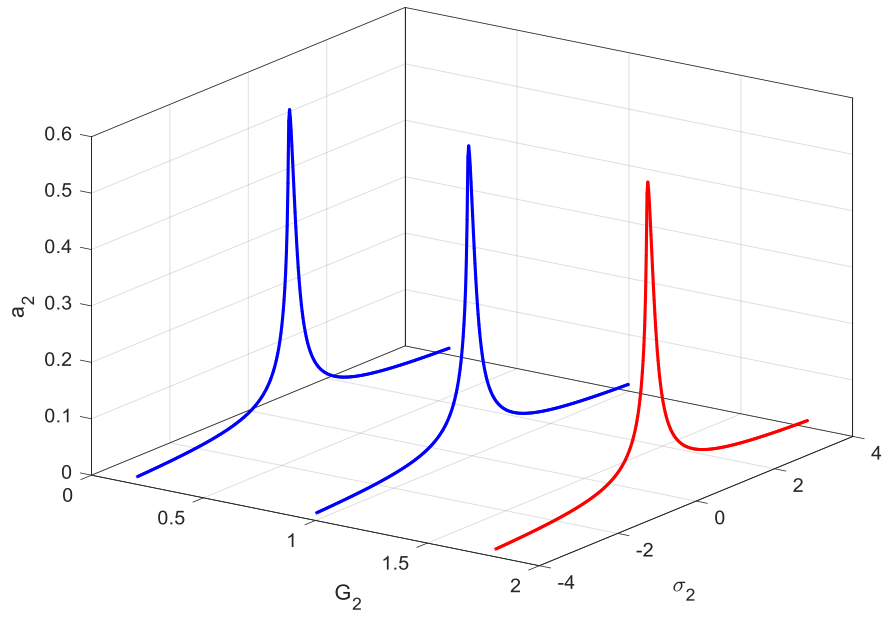

Figure 33. Three-dimensional frequency response of steady-state amplitude a_2 against detuning parameter σ_2 and gain coefficient G_2.

4.8. Bifurcation analysis with respect to force excitation amplitude

Bifurcation diagrams are made by altering the force excitation amplitude F while keeping an eye on the steady-state response maxima in both orthogonal directions to investigate the nonlinear dynamic behavior of the scheme under increased external excitation. These diagrams provide critical insight into transitions between periodic, multi-periodic, and chaotic motions, as well as the onset of instability and coexistence of multiple attractors. The bifurcation procedure is carried out by numerically integrating the governing nonlinear equations of motion for each value of F after discarding transient responses. The local maxima of the steady-state displacement signals are then recorded and plotted against the excitation amplitude. This approach enables clear identification of qualitative changes in system dynamics as the forcing level increases.

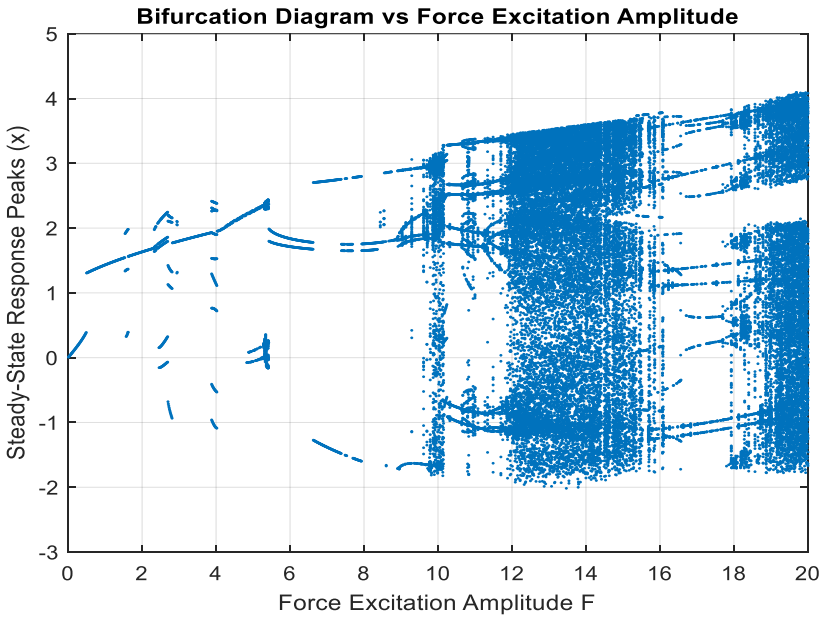

Figure 34. Bifurcation diagram of steady-state displacement peaks in the x-direction versus force excitation amplitude F, showing transitions from periodic motion to multi-periodic and chaotic responses.

Dynamic response in the x-direction

Figure 34 illustrates the bifurcation structure of the steady-state displacement peaks in the x-direction as a function of the force excitation amplitude. At low excitation levels, the system exhibits a stable single-period response characterized by a unique peak for each forcing value, indicating synchronous motion with the excitation frequency. As excitation amplitude F increases, the response experiences a sequence of bifurcations manifested by the splitting of response branches. These bifurcations indicate the emergence of multi-periodic oscillations and quasi-periodic behavior. Beyond a critical excitation threshold, a dense distribution of response peaks is observed, which is a signature of chaotic motion. The wide spread of points in this region reflects strong sensitivity to initial conditions and pronounced nonlinear effects induced by magnetic force nonlinearity and controller

interaction. Furthermore, the coexistence of multiple response branches over certain excitation intervals suggests the presence of multi-stability, where different attractors can exist for the same parameter value depending on initial conditions. This phenomenon is particularly relevant for practical operation, as it may lead to sudden jumps between distinct vibration states.

Dynamic response in the y-direction

The corresponding bifurcation diagram for the y-direction is presented in Figure 35. Similar to the x-direction, the response initially remains periodic at low excitation amplitudes. However, the onset of nonlinear behavior occurs at different forcing levels, reflecting anisotropy and coupling effects inherent in the system dynamics. With increasing excitation amplitude, the y-direction response exhibits pronounced branching and widening of the bifurcation structure. The appearance of scattered points over a broad amplitude range indicates a strong chaotic regime, which is more extensive than that observed in the x-direction. This difference highlights the influence of directional stiffness asymmetry and nonlinear coupling on the system's stability characteristics. Notably, regions of intermittent behavior are observed, where periodic windows are embedded within chaotic bands. Such behavior is typical of strongly nonlinear systems and confirms the complex interplay between excitation energy, nonlinear restoring forces, and control action. Finally, the bifurcation analyses in both directions demonstrate that increasing the force excitation amplitude can drive the system from stable periodic oscillations to chaotic motion through a sequence of nonlinear transitions. Moreover, the differences between the x- and y-direction responses emphasize the importance of considering multidirectional dynamics when assessing stability and performance. These results provide a solid foundation for further investigation using Lyapunov exponents, basins of attraction, and control parameter optimization to suppress undesirable chaotic vibrations.

Directional stiffness asymmetry can contribute to sudden rotor levitation failure, especially under certain operating conditions. The bifurcation analysis presented in the paper provides insights into how such asymmetries can lead to complex and unstable dynamic behaviors.

The bifurcation diagrams for the x and y directions (Figures 34 and 35) show that the system's response to increasing excitation amplitude is different in each direction. This difference is a direct consequence of the directional stiffness asymmetry and nonlinear coupling in the AMB system. The key observations are:

- Different bifurcation paths: The system follows different bifurcation paths in the x and y directions, indicating that the onset of instability and the transition to chaotic motion occur at different forcing levels for each direction. This anisotropy can lead to unpredictable and complex rotor dynamics.
- More extensive chaos in the y-direction: The bifurcation diagram for the y-direction shows a more extensive chaotic regime compared to the x-direction. This suggests that the system is more susceptible to instability in the y-direction, which could be a critical factor in levitation failure.
- Multi-stability and jumps: The presence of multi-stability, where multiple attractors coexist for the same parameter values, means that the rotor can suddenly jump between vibration states. A sudden jump to a high-amplitude oscillation state could exceed the bearing's capacity and lead to a loss of levitation.

In a real-world scenario, directional stiffness asymmetry can arise from various factors, including

manufacturing tolerances, uneven magnetic fields, and variations in the control currents. If the rotor is subjected to a disturbance that excites the more unstable direction, the resulting high-amplitude oscillations could lead to a catastrophic failure of the levitation system. Therefore, it is crucial to consider the effects of directional stiffness asymmetry in the design and control of AMB systems to ensure their safe and reliable operation.

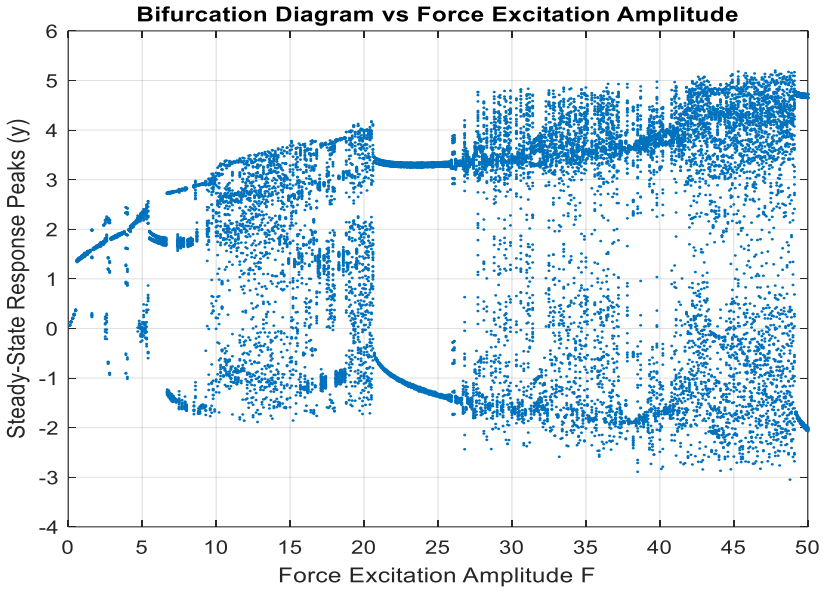

Figure 35. Bifurcation diagram of steady-state displacement peaks in the y-direction versus force excitation amplitude F, illustrating periodic, multi-periodic, intermittent, and chaotic response regimes.

4.9. Sensitivity analysis of controller gains

To evaluate the robustness of the proposed NPDCVF controller against variations in control parameters, a sensitivity analysis is performed by varying the proportional ($p_n, n=1,2$), derivative ($d_n, n=1,2$), and cubic feedback ($G_n, n=1,2$) gains by 20% around their nominal values for both vibration modes. For this analysis, I focus on the primary resonance conditions ($\Omega \cong \omega_1$, $\Omega \cong \omega_2$), where the system is most susceptible to external excitations.

4.9.1. First-mode sensitivity analysis

Figure 36 illustrates the impact of gain variations on the first-mode maximum vibration amplitude (a_1) and the effective damping ratio ($\zeta_{eff,1}$). The results demonstrate that the NPDCVF controller maintains stable and effective vibration suppression across the 20% range. Specifically, increasing the derivative (d_1) and cubic feedback (G_1) gains leads to a slight increase in the effective damping ratio,

which further reduces the vibration amplitude. Conversely, the system exhibits minimal sensitivity to variations in the proportional gain (p_1), highlighting the dominant role of the nonlinear cubic velocity feedback in providing robust damping, as shown in Table 2.

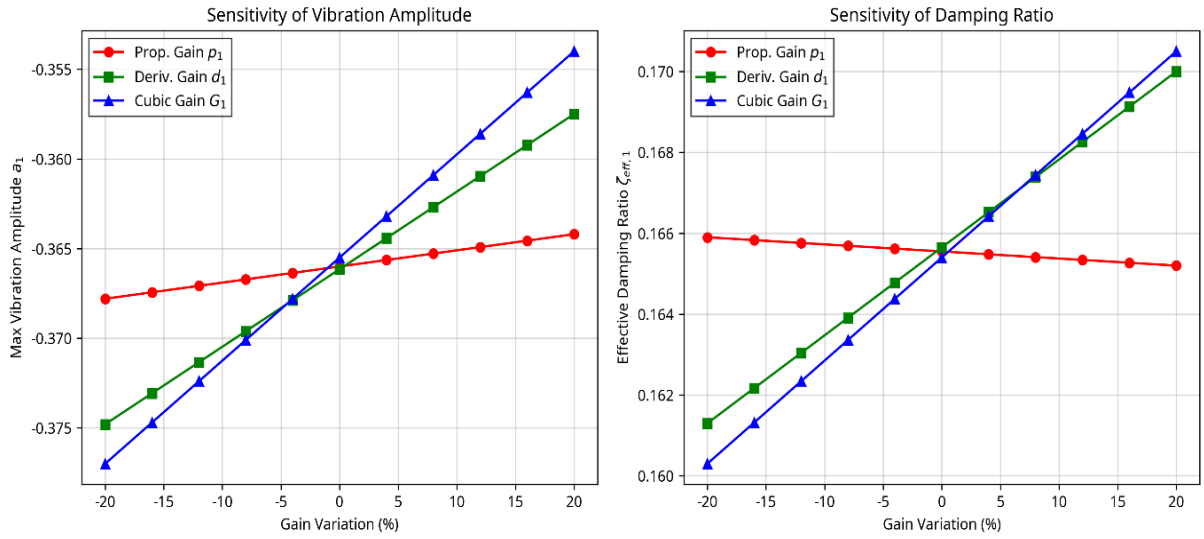

Figure 36. Sensitivity of (a) maximum vibration amplitude a_1 and (b) effective damping ratio $\zeta_{eff,1}$ to 20% variations in proportional (p_1), derivative (d_1), and cubic feedback (G_1) gain.

Table 2. Sensitivity of maximum first vibration amplitude and effective damping ratio.

Parameter variation	Mode 1 amplitude (a_1)	Mode 1 damping ratio ($\zeta_{eff,1}$)
Nominal value	0.3661	0.1656
Gain +20%	0.3585–0.3642	0.1670–0.1705
Gain –20%	0.3678–0.3775	0.1603–0.1652

4.9.2. Second-mode sensitivity analysis

The sensitivity analysis for the second mode is presented in Figure 37. Similar to the first mode, the second-mode amplitude (a_2) and effective damping ratio ($\zeta_{eff,2}$) remain consistently stable under gain variations. The NPDCVF controller effectively suppresses second-mode resonance, with the damping ratio showing a high degree of robustness. The results confirm that the proposed control strategy is not only effective but also highly resilient to parameter uncertainties in horizontal and vertical vibration directions, as demonstrated in Table 3.

Table 3. Sensitivity of maximum second vibration amplitude and effective damping ratio.

Parameter variation	Mode 2 amplitude (a_2)	Mode 2 damping ratio ($\zeta_{eff,2}$)
Nominal value	0.2609	0.2393
Gain +20%	0.2619–0.2669	0.2403–0.2429
Gain –20%	0.2549–0.2599	0.2357–0.2383

The stability of the steady-state responses and the consistent vibration attenuation over a wide range of gain values confirm the robustness of the NPDCVF control strategy. These findings suggest that the controller is well-suited for practical applications where precise tuning of control gains may be challenging due to component tolerances or environmental changes.

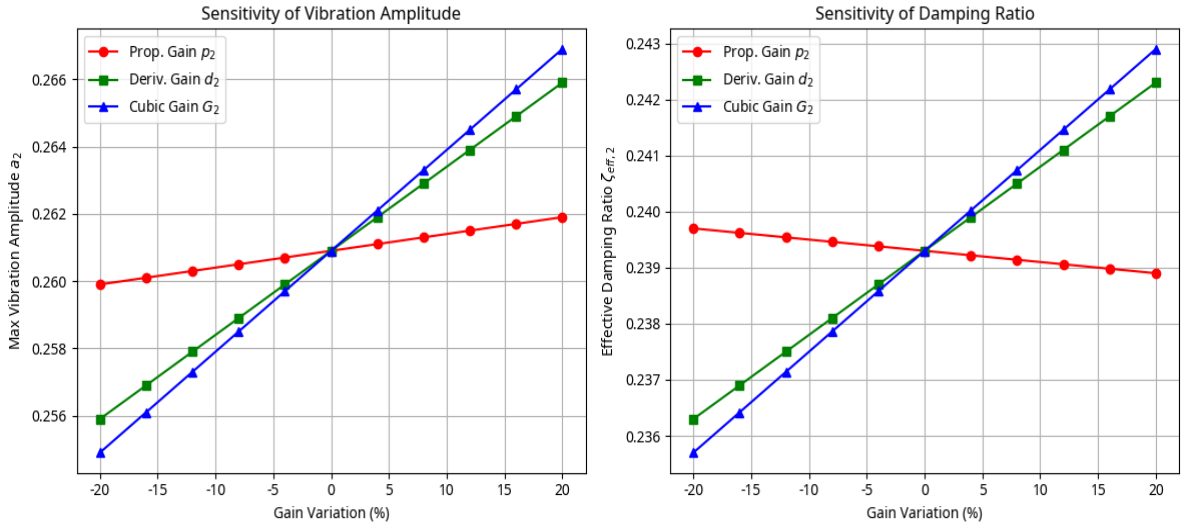

Figure 37. Sensitivity of (a) maximum vibration amplitude a_2 and (b) effective damping ratio $\zeta_{eff,2}$ to 20% variations in proportional (p_2), derivative (d_2), and cubic feedback (G_2) gain.

5. Conclusions

In this research, a 12-pole AMB framework operating close to the primary resonance condition and subjected to mixed excitations was thoroughly examined in terms of nonlinear dynamics and control. The NPDCVF controller was proposed and thoroughly assessed and compared to a number of proven control techniques. The analytical, numerical, and nonlinear dynamical investigations lead to the following important findings:

[1] Modeling and analytical validation: A comprehensive nonlinear mathematical model of the twelve-pole AMB system was created, taking dynamic coupling, rotor eccentricity, and magnetic force nonlinearities into consideration. The 4RK approach provided highly precise numerical verification of the approximate analytical solutions provided by the MTSA.

[2] Superior controller performance: The better performance of the NPDCVF controller was

shown by a methodical comparison with traditional control techniques (PD, IRC, PPF, and NIPPF). Time-domain responses demonstrated that, even in the presence of considerable external disturbances and parameter uncertainties, the NPDCVF method offered the fastest vibration attenuation, greatly reduced settling time, and low overshoot. The synergistic combination of linear PD action and nonlinear cubic velocity feedback, which effectively adjusts damping characteristics to vibration amplitude, is responsible for this improved performance.

[3] Effective resonance suppression: The NPDCVF controller significantly lowers resonant peak amplitudes and flattens the frequency-response curves, according to frequency-response measurements. Jump phenomena and hysteresis areas were significantly reduced as a result of the backbone curves' clear suppression of nonlinear hardening and softening effects. As a result, the operational frequency range linked to steady periodic replies was greatly increased, improving the AMB system's safe working bandwidth.

[4] Frequency-response characteristics and resonance suppression: In comparison to the other controllers, frequency-response tests showed that the NPDCVF controller significantly lowers resonant peak amplitudes and flattens the frequency-response curves. Jump phenomena and hysteresis areas were significantly reduced as a result of the backbone curves' clear suppression of nonlinear hardening and softening effects. Consequently, the AMB system's safe operating bandwidth was increased by greatly expanding the operational frequency range linked to reliable periodic replies.

[5] Enhanced stability regions and bifurcation control: The capacity of the NPDCVF controller to successfully postpone the start of bifurcations was demonstrated by bifurcation diagrams that were created with regard to the force excitation amplitude. Unlike conventional controllers, which showed huge unstable regions and chaotic attractors, it greatly reduced the extent of unstable regions and maintained stable single-period motion throughout a far broader excitation range in the x- and y-directions.

[6] Mitigation of directional asymmetry: The NPDCVF controller successfully reduced the directional asymmetry and coupling effects seen in AMB dynamics, according to comparative assessments of the x- and y-direction responses. It consistently suppressed nonlinear instabilities and produced more symmetric stability regions by providing balanced damping in both directions.

In conclusion, this study shows that a strong and efficient method for managing nonlinear vibrations in twelve-pole AMB systems is the nonlinear proportional–derivative cubic velocity feedback controller. The study provides a thorough framework for stability evaluation and control design of large AMB systems by combining analytical modeling, frequency-response analysis, and sophisticated nonlinear dynamics methods.

Practical implications and future work

From a practical perspective, the demonstrated capabilities of the NPDCVF controller strongly suggest its potential to enhance the reliability and safety of AMB-supported rotating machinery. By preventing sudden transitions to unstable or chaotic motion, and providing an enlarged stable operating region with robust performance under uncertainties, the controller is highly suitable for high-speed and high-precision rotor applications. In future research endeavors, I will focus on experimental validation of the NPDCVF scheme, adaptive tuning of its parameters, multi-mode resonance analysis, and real-time implementation on high-speed rotor test rigs to further solidify its industrial applicability.

Appendix

$$R_{11}=\frac{\partial a_1'}{\partial a_1}=-\frac{1}{2}\left[\mu_{10}+d_1\right]-\frac{3}{8}\left[\alpha_6-3\mu_2+3G_1\omega_1^2\right]a_1^2\ ,$$

$$R_{12}=\frac{\partial a_1'}{\partial \gamma_1}=\frac{F}{2\omega_1}\sin\gamma_1\ ,$$

$$R_{13}=\frac{\partial a_1'}{\partial a_2}=0,$$

$$R_{14}=\frac{\partial a_1'}{\partial \gamma_2}=0,$$

$$R_{21}=\frac{\partial \gamma_1'}{\partial a_1}=\frac{\sigma_1}{a_1}-\left[\frac{9\omega_1}{8}\mu_3+\frac{9}{8\omega_1}\alpha_2+\frac{9}{8\omega_1}\alpha_5+\frac{3\omega_1}{8}\alpha_7\right]a_1-\frac{p_1}{2a_1\omega_1}\ ,$$

$$R_{22}=\frac{\partial \gamma_1'}{\partial \gamma_1}=-\frac{F}{2a_1\omega_1}\sin\gamma_1,$$

$$R_{23}=\frac{\partial \gamma_1'}{\partial a_2}=0,$$

$$R_{24}=\frac{\partial \gamma_1'}{\partial \gamma_2}=0,$$

$$R_{31}=\frac{\partial a_2'}{\partial a_1}=0,$$

$$R_{32}=\frac{\partial a_2'}{\partial \gamma_1}=0,$$

$$R_{33}=\frac{\partial a_2'}{\partial a_2}=-\frac{3}{8}\left[\beta_7-3\mu_2+3G_2\omega_2^2\right]a_2^2-\frac{1}{2}\left[\mu_{10}+d_2\right],$$

$$R_{34}=\frac{\partial a_2'}{\partial \gamma_2}=\frac{F}{2\omega_2}\cos\gamma_2,$$

$$R_{41}=\frac{\partial \gamma_2'}{\partial a_1}=0\ ,$$

$$R_{42}=\frac{\partial \gamma_2'}{\partial \gamma_1}=0\ ,$$

$$R_{43}=\frac{\partial\gamma_2'}{\partial a_2}=\frac{\sigma_2}{a_2}--\left[\frac{9\omega_2}{8}\mu_3+\frac{9}{8\omega_2}\beta_2+9\beta_6+\frac{3\omega_2}{8}\beta_8\right]a_2-\frac{p_2}{a_2\omega_2},$$

$$R_{44}=\frac{\partial\gamma_2'}{\partial\gamma_2}=\text{戋}\frac{F}{2a_2\omega_2}\cos\gamma_2,$$

$$\rho_1=-R_{44}-R_{33}-R_{22}-R_{11},$$

$$\begin{aligned}\rho_2=&R_{11}R_{44}+R_{11}R_{33}+R_{11}R_{22}+R_{22}R_{44}+R_{22}R_{33}+R_{33}R_{44}-R_{21}R_{12}-R_{31}R_{13}-R_{41}R_{14}\\&-R_{34}R_{43}-R_{32}R_{23}-R_{42}R_{24},\end{aligned}$$

$$\begin{aligned}\rho_3=&R_{11}R_{32}R_{23}-R_{31}R_{12}R_{23}-R_{11}R_{22}R_{44}-R_{42}R_{23}R_{34}+R_{31}R_{22}R_{13}+R_{32}R_{23}R_{44}-R_{11}R_{22}R_{33}-R_{32}R_{43}R_{24}\\&-R_{21}R_{32}R_{13}+R_{11}R_{42}R_{24}+R_{31}R_{13}R_{44}+R_{21}R_{12}R_{44}-R_{21}R_{42}R_{14}+R_{42}R_{24}R_{33}+R_{21}R_{12}R_{33}-R_{11}R_{33}R_{44}\\&-R_{22}R_{33}R_{44}-R_{41}R_{12}R_{24}-R_{31}R_{43}R_{14}+R_{41}R_{22}R_{14}+R_{32}R_{34}R_{44}+R_{41}R_{14}R_{33}+R_{11}R_{34}R_{43}-R_{41}R_{13}R_{34},\end{aligned}$$

$$\begin{aligned}\rho_4=&-R_{41}R_{12}R_{23}R_{34}-R_{21}R_{12}R_{33}R_{44}+R_{11}R_{22}R_{33}R_{44}-R_{11}R_{42}R_{24}R_{33}+R_{21}R_{32}R_{13}R_{44}+R_{11}R_{32}R_{43}R_{24}\\&-R_{41}R_{32}R_{13}R_{24}+R_{41}R_{32}R_{23}R_{14}-R_{11}R_{22}R_{34}R_{43}+R_{21}R_{12}R_{34}R_{43}-R_{31}R_{12}R_{43}R_{24}-R_{21}R_{42}R_{13}R_{34}\\&-R_{21}R_{32}R_{43}R_{14}+R_{31}R_{12}R_{14}R_{44}+R_{31}R_{42}R_{13}R_{24}-R_{31}R_{42}R_{23}R_{14}+R_{21}R_{42}R_{14}R_{33}+R_{11}R_{42}R_{23}R_{34}\\&-R_{11}R_{32}R_{23}R_{44}+R_{31}R_{22}R_{43}R_{14}-R_{31}R_{22}R_{13}R_{44}+R_{41}R_{12}R_{24}R_{33}-R_{41}R_{22}R_{14}R_{33}+R_{41}R_{22}R_{13}R_{34}.\end{aligned}$$

Use of Generative-AI tools declaration

The author declares that he has not used Artificial Intelligence (AI) tools in the creation of this article.

Acknowledgments

The authors extend their appreciation to Prince Sattam bin Abdulaziz University for funding this research work through the project number (PSAU/ 2025/01/34093).

Data availability

All data generated or analyzed during this study are included in this published article.

Conflict of interest

The author declare that he has no known competing financial interests or personal relationships that could has appeared to influence the work reported in this paper.

References

1. G. Schweitzer, E. H. Maslen, *Magnetic bearings: Theory, design, and application to rotating machinery*, Berlin: Springer, 2009. https://doi.org/10.1007/978-3-642-00497-1

2. G. Schweitzer, H. Bleuler, A. Traxler, *Active magnetic bearings: Basics, properties, and applications of active magnetic bearings*, Zurich: vdf Hochschulverlag AG an der ETH, 1994.
3. H. Lv, H. Geng, J. Zhou, T. Du, H. Li, Structure design and optimization of thrust magnetic for the high-Speed motor, *2017 IEEE International Conference on Mechatronics and Automation (ICMA)*, 2017, 805–809. https://doi.org/10.1109/ICMA.2017.8015919
4. R. Q. Wu, W. Zhang, M. H. Yao, Nonlinear dynamics near resonances of a rotor-active magnetic bearings system with 16-pole legs and time varying stiffness, *Mech. Syst. Signal Process.*, **100** (2018), 113–134. https://doi.org/10.1016/j.ymssp.2017.07.033
5. R. Bakri, R. Nabergoj, F. Tondl, F. Verhulst, Parametric excitation in non-linear dynamics, *Int. J. Non-Linear Mech*., **39** (2004), 311–329. https://doi.org/10.1016/S0020-7462(02)00190-7
6. H. Abdelhafez, Resonance of a nonlinear forced system with two-frequency parametric and self-excitations, *Math. Comput. Simul*., **66** (2004), 69–83. https://doi.org/10.1016/j.matcom.2004.03.002
7. M. Kamel, H. S. Bauomy, Nonlinear behavior of a rotor-AMB system under multi-parametric excitations, *Meccanica*, **45** (2010), 7–22. https://doi.org/10.1007/s11012-009-9213-3
8. N. A. Saeed, W. A. El-Ganaini, Time-delayed control to suppress the nonlinear vibrations of a horizontally suspended Jeffcott-rotor system, *Appl. Math. Model*., **44** (2017), 523–539. https://doi.org/10.1016/j.apm.2017.02.019
9. K. Akash, K. P. Lijesh, V. Chittlangia, H. Hirani, Design and implementation of adaptive PID controller for active magnetic bearings, *International Conference on Advances in Tribology, ICAT14*, 2014.
10. N. A. Saeed, M. S. Mohamed, S. K. Elagan, J. Awrejcewicz, Integral resonant controller to suppress the nonlinear oscillations of a two-degree-of-freedom rotor active magnetic bearing system, *Processes*, **10** (2022), 271. https://doi.org/10.3390/pr10020271
11. A. Kandil, Y. S. Hamed, Tuned positive position feedback control of an active magnetic bearings system with 16 poles and constant stiffness, *IEEE Access*, **9** (2021), 73857–73872. https://doi.org/10.1109/ACCESS.2021.3080457
12. A. T. El-Sayed, H. S. Bauomy, NIPPF versus ANIPPF controller outcomes on semi-direct drive cutting transmission system in a shearer, *Chaos Solitons Fractals*, **156** (2022), 111778. https://doi.org/10.1016/j.chaos.2021.111778
13. Y. Ren, W. Ma, Dynamic analysis and PD control in a 12-pole active magnetic bearing system, *Mathematics*, **12** (2024), 2331. https://doi.org/10.3390/math12152331
14. I. I. H. Jawaid, Bifurcations in the response of a rigid rotor supported by load sharing between magnetic and auxiliary bearings, *Meccanica*, **46** (2011), 1341–1351. https://doi.org/10.1007/s11012-010-9395-8
15. J. C. Ji, A. Y. T. Leung, Non-linear oscillations of a rotor-magnetic bearing system under super harmonic resonance conditions, *Int. J. Non-Linear Mech.*, **38** (2003), 829–835. https://doi.org/10.1016/S0020-7462(01)00136-6
16. T. Inoue, Y. Sugawara, Nonlinear vibration analysis of a rigid rotating shaft supported by the magnetic bearing (influence of the integral feedback in the PID control of the vertical shaft), *J. Syst. Des. Dyn.*, **4** (2010), 471–483. https://doi.org/10.1299/jsdd.4.471
17. H. C. Sung, J. B. Park, Y. H. Joo, Robust fuzzy controller for active magnetic bearing system with 6-DOF, *J. Korean Inst. Intell. Syst.*, **22** (2012), 267–272. https://doi.org/10.5391/JKIIS.2012.22.3.267

18. G. Zhang, G. Xi, Vibration control of a time-delayed rotor-active magnetic bearing system by time-varying stiffness, *Int. J. Appl. Mech.*, **14** (2022), 2250007. https://doi.org/10.1142/S1758825122500077
19. H. C. Wu, L. Zhang, J. Zhou, Y. F. Hu, Dynamic analysis and vibration control of a rotor-active magnetic bearings system with base motion, *J. Vib. Control*, **30** (2023), 2697–2708. https://doi.org/10.1177/10775463231183190
20. X. Xu, Y. Liu, Q. Han, A universal dynamic model and solution scheme for the electrical rotor system with wide range of eccentricity, *Int. J. Non-Linear Mech.*, **152** (2023), 104402. https://doi.org/10.1016/j.ijnonlinmec.2023.104402
21. C. W. Chang, L. M. Chu, T. C. Chen, H. T. Yau, Nonlinear dynamic of turbulent bearing-rotor system under quadratic damping with HSFD and active control, *J. Braz. Soc. Mech. Sci. Eng.*, **46** (2024), 123. https://doi.org/10.1007/s40430-024-04691-7
22. C. Wang, C. C. Liu, S. K. Cao, L. Sun, Nonlinear vibration control of magnetic bearing system considering positive and negative stiffness, *J. Vib. Control*, **31** (2024), 796–806. https://doi.org/10.1177/10775463241233616
23. M. Eissa, M. Kamel, H. S. Bauomy, Dynamics of an AMB-rotor with time varying stiffness and mixed excitations, *Meccanica*, **47** (2012), 585–601. https://doi.org/10.1007/s11012-011-9469-2
24. Y. A. Amer, U. H. Hegazy, Resonance behavior of a rotor active magnetic bearing with time-varying stiffness, *Chaos Solitons Fractals*, **34** (2007), 1328–1345. https://doi.org/10.1016/j.chaos.2006.04.040
25. M. Kamel, H. S. Bauomy, Nonlinear oscillation of a rotor-AMB system with time-varying stiffness and multi-external excitations, *J. Vib. Acoust.*, **131** (2009), 031009. https://doi.org/10.1115/1.3085884
26. W. Zhang, J. W. Zu, F. X. Wang, Global bifurcations and chaos for a rotor-active magnetic bearing system with time varying stiffness, *Chaos Solitons Fractals*, **35** (2008), 586–608. https://doi.org/10.1016/j.chaos.2006.05.095
27. W. Zhang, J. W. Zu, Transient and steady nonlinear responses for a rotor-active magnetic bearings system with time-varying stiffness, *Chaos Solitons Fractals*, **38** (2008), 1152–1167. https://doi.org/10.1016/j.chaos.2007.02.002
28. X. D. Yang, H. Z. An, Y. J. Qian, W. Zhang, M. H. Yao, Elliptic motions and control of rotors suspending in active magnetic bearings, *J. Comput. Nonlinear Dyn.*, **11** (2016), 054503. https://doi.org/10.1115/1.4033659
29. W. Zhang, M. H. Yao, X. P. Zhan, Multi-pulse chaotic motions of a rotor-active magnetic bearing system with time varying stiffness, *Chaos Solitons Fractals*, **27** (2006), 175–186. https://doi.org/10.1016/j.chaos.2005.04.003
30. J. Li, Y. Tian, W. Zhang, S. F. Miao, Bifurcation of multiple limit cycles for a rotor-active magnetic bearings system with time-varying stiffness, *Int. J. Bifurcation Chaos*, **18** (2008), 755–778. https://doi.org/10.1142/S021812740802063X
31. J. Li, Y. Tian, W. Zhang, Investigation of relation between singular points and number of limit cycles for a rotor- AMBs system, *Chaos Solitons Fractals*, **39** (2009), 1627–1640. https://doi.org/10.1016/j.chaos.2007.06.044
32. J. Awrejcewicz, L. P. Dzyubak, Chaos caused by hysteresis and saturation phenomenon in 2-DOF vibrations of the rotor supported by the magneto- hydrodynamic bearing, *Int. J. Bifurcation Chaos*, **21** (2011), 2801–2823. https://doi.org/10.1142/S0218127411030155

33. N. A. Saeed, M. Eissa, W. A. El-Ganaini, Nonlinear oscillations of rotor active magnetic bearing systems, *Nonlinear Dyn.*, **74** (2013), 1–20. https://doi.org/10.1007/s11071-013-0967-8
34. J. I. Inayat-Hussain, Geometric coupling effects on the bifurcations of a flexible rotor response in active magnetic bearings flexible rotor response in active magnetic bearings, *Chaos Solitons Fractals*, **41** (2009), 2664–2671. https://doi.org/10.1016/j.chaos.2008.09.041
35. N. A. Saeed, W. A. El-Ganaini, Time-delayed control to suppress the nonlinear vibrations of a horizontally suspended Jeffcott-rotor system, *Appl. Math. Modell.*, **44** (2017), 523–539. https://doi.org/10.1016/j.apm.2017.02.019
36. M. R. Ghazavi, Q. Sun, Bifurcation onset delay in magnetic bearing systems by time varying stiffness, *Mech. Syst. Signal Process.*, **90** (2017), 97–109. https://doi.org/10.1016/j.ymssp.2016.12.016
37. R. Ebrahimi, M. Ghayour, H. M. Khanlo, Effects of some design parameters on bifurcation behavior of a magnetically supported coaxial rotor in auxiliary bearings, *Eng. Comput.*, **34** (2017), 2379–2395. https://doi.org/10.1108/EC-04-2017-0141
38. A. Kandil, Nonlinear dynamic behavior, impact suppression, and stability control of rotor active magnetic bearing systems: A comparative study of fixed and adjustable surplus current strategies, *Eur. J. Mech. A Solids*, **116** (2026), 105928. https://doi.org/10.1016/j.euromechsol.2025.105928
39. H. S. Bauomy, A. T. El-Sayed, T. S. Amer, M. K. Abohamer, Negative derivative feedback control and bifurcation in a two-degree-of-freedom coupled dynamical system, *Chaos Solitons Fractals*, **193** (2025), 116138. https://doi.org/10.1016/j.chaos.2025.116138
40. M. K. Abohamer, T. S. Amer, A. A. Galal, M. A. Darweesh, A. Arab, T. A. Bahnasy, Nonlinear oscillations of a lumped system with series spring, piezoelectric device, and feedback controller, *Sci. Rep.*, **15** (2025), 14642. https://doi.org/10.1038/s41598-025-97173-2
41. T. S. Amer, G. M. Moatimid, S. K. Zakria, A. A. Galal, Vibrational and stability analysis of planar double pendulum dynamics near resonance, *Nonlinear Dyn.*, **112** (2024), 21667–21699. https://doi.org/10.1007/s11071-024-10169-x
42. S. Ghanem, T. S. Amer, W. S. Amer, S. Elnaggar, A. A. Galal, Analyzing the motion of a forced oscillating system on the verge of resonance, *J. Low Freq. Noise Vib. Act. Control*, **42** (2023), 563–578. https://doi.org/10.1177/14613484221142182
43. A. H. Nayfeh, *Introduction to perturbation techniques*, New York: Wiley, 1993.
44. A. H. Nayfeh, *Perturbation methods*, New York: Wiley, 1973.
45. A. H. Nayfeh, D. T. Mook, *Nonlinear oscillations*, New York: Wiley, 1979.
46. A H. Nayfeh, Resolving Controversies in the Application of the Method of Multiple Scales and the Generalized Method of Averaging, *Nonlinear Dyn.*, **40** (2005), 61–102. https://doi.org/10.1007/s11071-005-3937-y

AIMS Press